

A network-based flow accumulation algorithm for point clouds: Facet-Flow Networks (FFN)

Aljoscha Rheinwalt¹, Bedartha Goswami^{1*}, Bodo Bookhagen¹

¹Institute of Geoscience, University of Potsdam, Potsdam, Germany

Key Points:

- Specific catchment area estimation from irregular point-cloud data by triangulated irregular networks (TINs).
- Efficient and innovative sink treatment to generate hydrologically correct flow estimates from point-cloud data.
- Comparative study on accuracy gains in specific catchment area estimations with an increase in resolution of the digital topography.

This article has been accepted for publication and undergone full peer review but has not been through the copyediting, typesetting, pagination and proofreading process which may lead to differences between this version and the Version of Record. Please cite this article as doi: 10.1029/2018JF004827

*Current affiliation: Potsdam Institute for Climate Impact Research, Potsdam, Germany

Corresponding author: Aljoscha Rheinwalt, aljoscha.rheinwalt@uni-potsdam.de

Abstract

Flow accumulation algorithms estimate the steady state of flow on real or modeled topographic surfaces and are crucial for hydrological and geomorphological assessments, including delineation of river networks, drainage basins, and sediment transport processes. Existing flow accumulation algorithms are typically designed to compute flows on regular grids and are not directly applicable to arbitrarily sampled topographic data such as lidar point clouds. In this study we present a random sampling scheme that generates homogeneous point densities, in combination with a novel flow path tracing approach — the Facet Flow Network (FFN) — that estimates flow accumulation in terms of specific catchment area (*SCA*) on triangulated surfaces. The random sampling minimizes biases due to spatial sampling and the FFN allows for direct flow estimation from point clouds. We validate our approach on a Gaussian hill surface and study the convergence of its *SCA* compared to the analytical solution. Here, our algorithm outperforms the Multiple Flow Direction (MFD) algorithm, which is optimized for divergent surfaces. We also compute the *SCA* of a 6 km² steep, vegetated catchment on Santa Cruz Island, California, based on airborne-lidar point-cloud data. Point-cloud based *SCA* values estimated by our method compare well with those estimated by the D_{∞} or MFD algorithm on gridded data. The advantage of computing *SCA* from point clouds becomes relevant especially for divergent topography and for small drainage areas: these are depicted with much more detail due to the higher sampling density of point clouds.

1 Introduction

Recent advances in generating high-resolution topographic data have increased the demand on computing resources, new algorithms, and techniques [Roering *et al.*, 2013; Larsen *et al.*, 2016]. Methods such as lidar and Structure-from-Motion generate densely-sampled ‘point clouds’ that are then used for a wide range of hydrologic and tectono-geomorphic applications (see e.g., Hurst *et al.* [2012], Perroy *et al.* [2012], Neely *et al.* [2017], Hilly and Arrowsmith [2008], Meigs [2013], Arrowsmith and Zielke [2009], Passalacqua *et al.* [2010], Passalacqua *et al.* [2015], Tarolli *et al.* [2009]). A typical airborne lidar data set can contain on the order of 10 points per square meter, leading to a billion points for a study site of 100 square kilometers [Roering *et al.*, 2013; Passalacqua *et al.*, 2015]. Before being used in geomorphic and hydrological analyses however, high resolution point-cloud data sets are often converted to Digital Elevation Models (DEMs) by ag-

44 gregating them to a regular, coarser grid (e.g., to a resolution of ≈ 1 grid point per square
45 meter). This is typically done in order to allow for more realistic computation times, po-
46 tentially reduce the impact of random errors in the measurements, and to gain analytical
47 tractability because of the regularity of the gridded estimates. Although there exist sev-
48 eral applications that are not severely impacted by the ‘gridding’ step, as they do not re-
49 quire the fine-scaled, sub-meter spatial resolution, we contend that the inherent data set
50 resolution—that of the point cloud itself—would allow more detailed insights into the hy-
51 drological features of the landscape. Geomorphic studies of ephemeral channels, channel
52 heads in dry areas with weak lithologies, landslide scarps and arroyo formation would all
53 benefit from sub-meter spatial resolution data. Existing approaches that are commonly
54 used to construct river-flow networks from elevation data sets, however, are not equipped
55 to handle point clouds directly, and require a DEM as a starting point of the analysis. Ad-
56 ditionally, DEMs usually have fewer pixels than the underlying point cloud in order to mit-
57 igate elevation uncertainties and to avoid interpolation artifacts [Florinsky, 1998; Oksanen
58 and Sarjakoski, 2006; Wechsler and Kroll, 2006; Wechsler, 2007].

59 In this study, we describe a network approach to perform flow accumulation on ir-
60 regularly spaced point clouds and provide a framework that links this method to existing,
61 grid-based flow accumulation techniques. In our approach, we generate a flow network
62 from the irregularly sampled point-cloud data set by representing the topographic surface
63 with a Triangulated Irregular Network (TIN). Such a representation of the topographic
64 surface assumes a linear model for elevations between measurements, which might not
65 be a valid approximation depending on the roughness of the terrain and the number of
66 measurements per square meter. However, since a TIN can be constructed from any arbi-
67 trary set of sampled points, our method is directly applicable to point-cloud data, which
68 yields the highest possible measurement densities. Despite the existence of flow accumu-
69 lation approaches on TINs, (see e.g., Jones *et al.* [1990]; Ivanov *et al.* [2004]; Zhou *et al.*
70 [2011]), we put forward an efficient and realistic approximation of flow on the surface of
71 the TIN facets themselves and hence refer to this network as Facet-Flow Network (FFN).
72 Our approximation is realistic because estimates converge to the analytical solution even
73 for terrain with diverging flow where flow partitioning is most important, and it is effi-
74 cient because our flow partitioning depends only on the local gradient and not on the full
75 evolution of the corresponding *stream tube*. We define a *stream tube* to be the flow path

76 bounded by the two flow lines originating at the boundary of that flow path's first facet.

77 The evolution of flow lines on TINs is determined by the gradient of its facets.

78 The underlying assumption in our flow path estimation is that rain falling onto the
79 triangulated surface (facet) of the TIN is transported from facet to facet as determined by
80 the local gradient, and thereby aggregates into channels and rivers that eventually drain
81 into one or more outlets. However, we do not consider variations in the flow density at the
82 sub-facet level. Water exiting a facet is considered to be homogeneously distributed along
83 the corresponding contour of the facet.

84 Although we are interested in a geometric terrain analysis in terms of drainage ar-
85 eas, the FFN approach could be extended for studies of hydrological modeling. Such a
86 hydrological model may analyze the flow propagation and its temporal evolution due to
87 variations of rainfall in time and space. However, assuming a constant rain rate [ms^{-1}], a
88 steady flow pattern will emerge, which can be expressed by the amount of water per time
89 [m^3s^{-1}] at each point on the topographic surface. Because we assume rainfall as spatially
90 homogeneous (i.e., the rain rate is the same at all locations) the flow can be studied in
91 terms of the total drainage area (*TDA*). For each point in space, the *TDA* is defined as
92 the size of the 2D surface area that drains into it. Note that the *TDA* at a chosen location
93 is not proportional to the area of the 3D surface upstream of that location, but it is rather
94 proportional to area of the *xy*-projection of the 3D surface. *TDA* is thus proportional to
95 water amounts that flow through the surface due to spatially homogeneous rainfall. How-
96 ever, although not implemented that way, our approach could as well be used to accumu-
97 late the 3D surface area of facets if a slope dependent *TDA* is desired.

98 *TDA* has been used by many hydrologic and geomorphologic applications to model
99 the flow of water and sediment [Montgomery and Foufoula-Georgiou, 1993; Tucker and
100 Bras, 1998; Rengers *et al.*, 2016]. However, *TDA* is inherently resolution dependent, mak-
101 ing it difficult to compare between data sets of different resolutions [Pelletier, 2010]. The
102 resolution dependence leads to biases in estimates for irregularly sampled data. The higher
103 the resolution, the smaller the grid cells or facets and the lower the *TDA*, because *TDA*
104 is an aggregated measure along the contour width of cells [Schoorl *et al.*, 2000; Zhou and
105 Liu, 2002; Erskine *et al.*, 2006]. Although our network-based approach also accumulates
106 flow to *TDA*, we use the specific catchment area (*SCA*), which is defined as *TDA* per
107 unit contour width. Hence, even though both *TDA* and *SCA* are directly estimated using

108 FFNs, *SCA* is unbiased even if the sampling density changes across the geographic re-
109 gion of interest and is therefore used throughout this study. An advantage of using FFNs
110 is that each facet has a well defined corresponding contour width and thus a more accu-
111 rate estimation of *SCA* can be directly calculated for high-spatial resolution data. For
112 other approaches it is often challenging to estimate *SCA* accurately because correspond-
113 ing contour widths are unknown or heuristically estimated in terms of effective contour
114 widths [Chirico *et al.*, 2005; Qin *et al.*, 2007; Pelletier, 2010]. Given a grid-based flow ac-
115 cumulation that allows multiple flow directions, the correct contour width inside channels
116 is the grid cell width. However, the more diverging the landscape, the higher the corre-
117 sponding contour width.

118 An additional advantage of the FFN approach is that it enables us to apply a novel
119 way to resolve sinks in the landscape. A sink in digital topography is a single cell, or
120 a group of grid cells that have no lower neighbor [O'Callaghan and Mark, 1984; Jen-
121 son and Domingue, 1988]. Instead of carving or filling sinks in digital topography (e.g.,
122 O'Callaghan and Mark [1984]; Rieger [1993]; Planchon and Darboux [2002]; Soille *et al.*
123 [2003]; Zhang *et al.* [2017]), we propose a fundamentally different approach that does not
124 alter the digital topography. We introduce new additional links into the flow network that
125 'tunnel' the flow out of sinks. This approach is more similar to sink carving than to sink
126 filling, in the sense that water is routed away from the bottom of sinks instead of over-
127 flowing the sink. High-resolution topography creates new challenges because the effect of
128 anthropogenic artifacts such as road embankments and bridges increases with increased
129 resolution. Similarly, at fine spatial scales, sinks exist in natural landscapes and high-
130 resolution topographic data will result in hydrologically disconnected landscapes. Part of
131 the difficulty arises from the problem of reliable point-cloud classification and the removal
132 of non-ground objects (i.e., vegetation, buildings) from a point cloud used for generating
133 digital topography. Specifically, classification inaccuracies in densely vegetated terrain will
134 introduce false point elevations which ultimately will result in surface-water flow obstruc-
135 tion. The FFN sink-tunneling approach mitigates some of these constraints.

136 In order to apply the FFN algorithm and demonstrate its usefulness, we validate
137 FFN *SCA* estimations of a Gaussian hill against the analytical solution of *SCA* and com-
138 pare the efficiency of our algorithm to that of the Multiple Flow Direction (MFD) algo-
139 rithm [Freeman, 1991; Pelletier, 2008]. We then analyze classified point-cloud data from
140 the steep and vegetated Pozo catchment of the Santa Cruz Island in southern California.

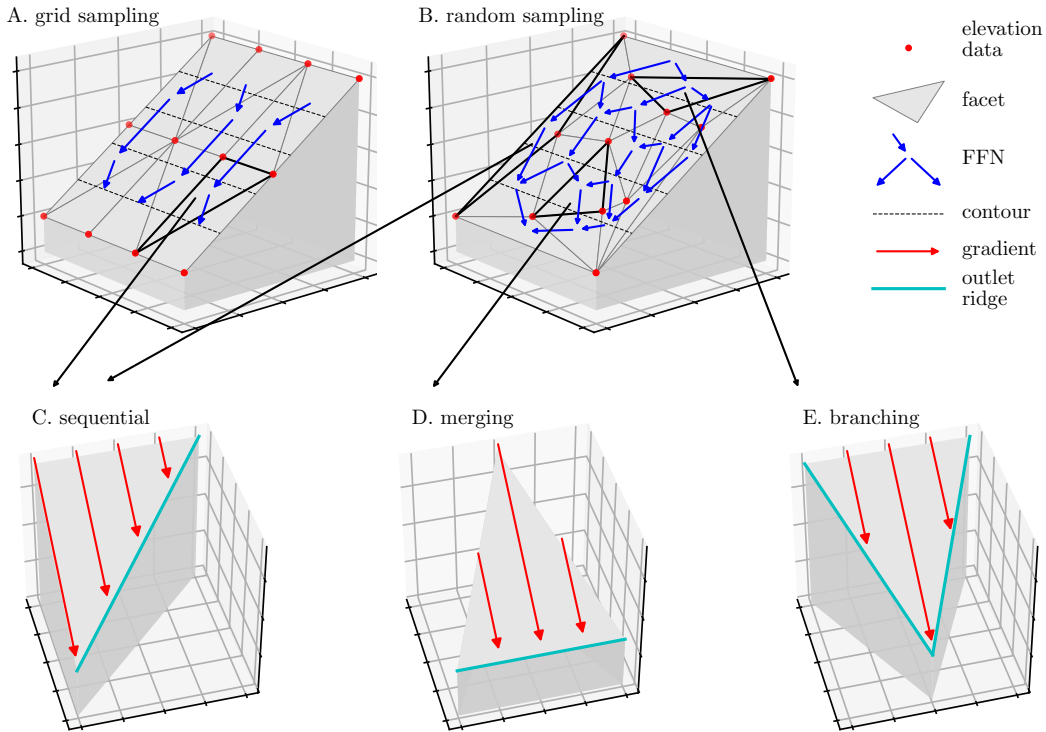
141 For the Pozo point cloud, we compare our FFN *SCA* to the one derived by MFD from a
 142 corresponding set of sink-filled 60 cm Digital Elevation Models (DEM) (see the Supple-
 143 mentary Material for comparisons to the D_∞ algorithm). Our findings suggest that FFN
 144 *SCA* estimations are more efficient and accurate than conventional *SCA* estimations from
 145 gridded data.

146 2 Methods

147 2.1 Facet-Flow Network (FFN) construction

48 We first construct a *Triangulated Irregular Network* (TIN) from all elevation mea-
 49 surements using a 2D Delaunay triangulation [Barber *et al.*, 1996]. Delaunay triangu-
 50 lation is applied to the projected, spatial coordinates (e.g. UTM Eastings and Northings) of
 51 the elevation measurements such that the resulting TIN is a unique nearest-neighbor net-
 52 work embedded in geographical space. Note that depending on coordinate systems and
 53 space the distance metric might change. For our applications, we consider Cartesian co-
 54 ordinates with Euclidean distances. We define *facets* as the triangular surfaces formed
 55 in the TIN that guide the flow of water. This is in contrast to existing approaches where
 56 flows are modeled along the edges of the TIN (e.g., Ivanov *et al.* [2004]). The flow direc-
 57 tion on a facet follows the gradient determined by the elevation values of its three corners.
 58 The flow has to exit at one or two sides of the facet and enters from corresponding neigh-
 59 boring facets. This determines a directed connection between facets, which we define as
 60 the directed links of the *Facet-Flow Network* (FFN) in which the facets are the network
 61 nodes. Since we obtain the TIN by Delaunay triangulation, the FFN is spatially structured
 62 as a Voronoi graph. This FFN can be seen as a drainage network, and since we assume
 63 the flow to be homogeneous along contours within facets, FFN links connect facets that
 64 drain into each other via flow lines. Accordingly, the FFN is a relational network and flow
 65 lines are not parallel to FFN links. We conceive FFN flow lines as flow paths following
 66 the gradient of the faceted surface of the TIN. This is in contrast to flow lines estimated
 67 at sub-pixel resolution by adjusting the flow path in the current grid cell according to the
 68 exit point in the previous grid cell [Zhou *et al.*, 2011].

69 We illustrate the concept of FFN using 12 elevation measurements on an inclined
 70 plane obtained by two different sampling schemes: (i) regular grid (Fig. 1 A) and (ii) ir-
 71 regular random sampling (Fig. 1 B). The gradient-determined flow pattern within a facet



¹⁷⁷ **Figure 1.** Two conceptual examples of 12 elevation measurements (red dots) on an inclined plane and their
¹⁷⁸ corresponding Facet-Flow Networks (FFNs, blue arrows) for regular grid sampling (A) and irregular random
¹⁷⁹ sampling (B). The gridded sampling leads to 12 facets and the random sampling to 18. All possible flow
¹⁸⁰ patterns for flow on facets are listed below. Sequential flow (C): the flow enters on one side, and exits on one.
¹⁸¹ Merging flow (D): the flow enters on two sides, and exits on one. Branching flow (E): the flow enters on one
¹⁸² side, and exits on two. Red arrows indicate the direction of the gradient and cyan colored ridges are those
¹⁸³ across which the flow exits the facet.

⁷² can be only one of three types, all of which manifest in the two conceptual samples shown
⁷³ in Fig. 1. The patterns are: (i) sequential (Fig. 1 C), the flow enters from one side and
⁷⁴ exits through another, (ii) merging (Fig. 1 D), the flow enters from two sides and ex-
⁷⁵ its through one, and (iii) branching (Fig. 1 E), the flow enters from one side and exits
⁷⁶ through the remaining two sides.

¹⁸⁴ These flow patterns arise because at each non-flat facet, the flow either enters the
¹⁸⁵ facet through one of its sides and exits either at one or both of the other remaining sides,
¹⁸⁶ or enters on two sides and exits on the remaining one. We note that perfectly flat facets
¹⁸⁷ occur only because of the finite elevation measurement precision. In that case, one can lift
¹⁸⁸ one corner of such a facet, while remaining within the bounds of elevation uncertainty.

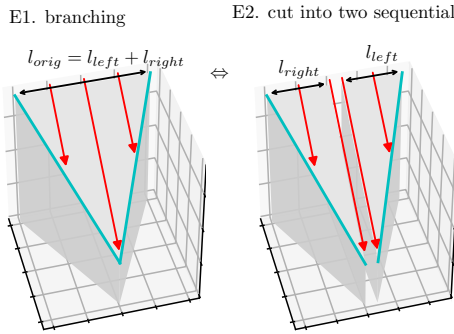


Figure 2. For FFN construction, we separate the branching flow (E1) into two sequential flow patterns (E2).

The equivalence of a facet with a branching flow pattern and its two corresponding sub-facets is obtained by dissecting the original flow pattern along the gradient that points to the lowest corner. I.e., the branching flow pattern can be routed with two parallel sequential flow patterns.

We detect flat facets while computing the gradient for each facet. In the FFN, each exit side is seen as an outgoing link, and in order to construct the entire FFN it suffices to focus only on these outgoing links. From the perspective of outgoing links, the sequential and merging flow patterns are equivalent as each of them have only one outgoing link. The branching flow pattern can in turn be seen as two parallel sequential flow patterns by dissecting the facet along the FFN flow line that passes through the lowest corner of the facet (Fig. 2). The dissection is unique, and it conserves both area and flow, i.e., the area of the original facet is equal to the sum of both sub-facet areas, and the flow routed through the original facet is equal to the sum of both flows that get routed through the two sub-facets. The conservation of flow holds because we assume homogeneous flow and the ridge length l_0 is conserved ($l_{orig} = l_{left} + l_{right}$, see Fig. 2). Although we are not dissecting branching facets in practice, each facet is seen as one node in the FFN, this perspective highlights how we accumulate the flow along branching facets.

2.2 Sinks and connecting facets via tunnels

We define a *sink* as a depression in the landscape where water accumulates and then either internally drains via sub-surface flow, evaporates, or overflows. Sinks are a common feature of elevation data sets at various spatial scales [O'Callaghan and Mark, 1984; Roering *et al.*, 2013]. Many sinks that are found in elevation datasets, such as tiny depressions which may cause puddles, are in fact an integral part of the geomorphic and hydrologic

signature of the landscape. That being said, one of the primary goals of a flow model is to route water through all parts of the landscape, including sinks, to one or more outlets.

Conventionally, in gridded datasets, the issue of sinks is resolved either by filling up the depression or by carving a channel through the surrounding landscape, resulting in a modified, ‘hydrologically-corrected’ landscape [O’Callaghan and Mark, 1984; Rieger, 1993; Planchon and Darboux, 2002; Zhang *et al.*, 2017]. Other approaches avoid this modification by directing flow uphill out of a sink towards the outlet of that sink [Wang *et al.*, 2009; Du *et al.*, 2017]. Here, we propose an approach that modifies the FFN without a modification of the underlying TIN. Instead of changing the elevation of the landscape, we introduce *tunnels* — new links that tunnel through sink-forming barriers (Fig. 3). In FFNs, sinks cause *link cycles* and to introduce tunnels, we detect facets that are part of a cycle, remove the links that cause the cycle (cyan links in Fig. 3), and place new links that connect the sink with lower facets nearby (dashed magenta links in Fig. 3). In other words, for each cycle-causing link, starting at the facet where the link originates, we perform a breadth-first search for the next closest facet which has its highest point below the level of the bottom of the sink. This results in two tunnels for each facet forming the sink, which may or may not connect to the same facet. This is clear from Fig. 3 B, where the facet on the far side has tunnels that end up in different locations, whereas for all the other facets forming the sink, both tunnels from each of them link to the same facet. Similar to filling or carving algorithms, a threshold of maximum distance or elevation drop can be included, in order to exclude nonphysical tunneling.

We acknowledge that a small and shallow depression in the landscape might rather overflow, than drain via sub-surface flow, but in such cases tunnels will be short and shallow with differences between the two cases being negligible in terms of drainage area. We note that sub-surface flow is typically orders of magnitude slower than overland flow, but since we focus on the steady state of flow, flow speeds are irrelevant. Fundamentally, the question whether a sink is rather filled or drained via sub-surface flow, is answered by a full hydrological model which is beyond the scope of this study. For our application to airborne lidar data most sinks are very shallow and sampling dependent, i.e., we conclude that all areas drain and that sinks are spurious (see Supplementary Material Fig. S7, S8). Despite the use of tunnels in our approach, we aim at creating a hydrologically-corrected flow on a TIN that can be used to study upslope areas, river profiles, and similar geomorphic metrics.

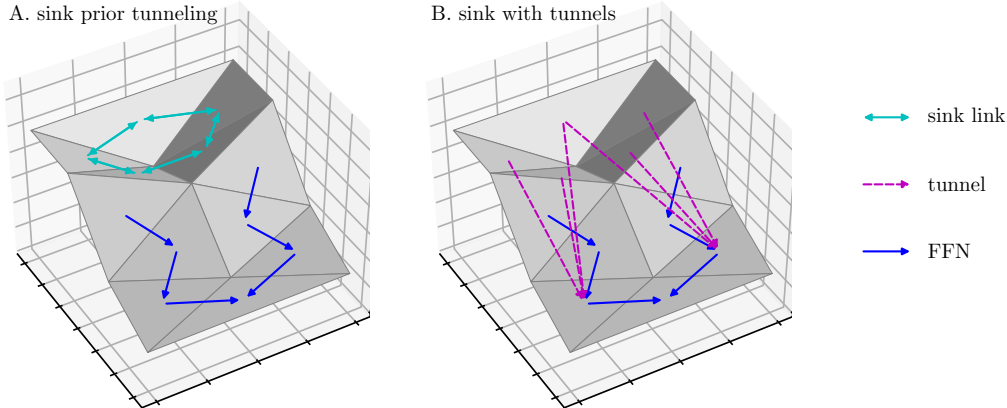


Figure 3. Schematic of a sink causing *cycles* (solid cyan arrows) and the corresponding *tunnels* (dashed magenta arrows) that route the flow below the surface to lower facets. *Cycles* are not physical and are replaced by *tunnels*. For display purposes, all links are drawn on top of the surface even if they are underneath or behind.

Additionally, we note that in the FFN, cycles of length two occur that are not due to physical sinks but simply because two neighboring facets point towards each other such as the pages of a half open book (cf. only two facets connected by a cyan link as in Fig. 3). This is also dealt with in the same way as in the case of sinks, only that we now search for the nearest facet lower than the lowest point of their common side. This has to be a facet whose highest corner is the lowest point of that common side. These new links represent the flow along the common side which drains into the next lower facet.

2.3 Flow accumulation and FFN-derived SCA

In landscapes and their static consideration, flow is often expressed as flow accumulation or drainage area and not in units of m^3s^{-1} [O'Callaghan and Mark, 1984; Jenkinson and Domingue, 1988; Chirico et al., 2005; Gallant and Hutchinson, 2011]. In that sense, the flow that exits a facet possibly comes from two areas: the upstream drainage area which is the flow that is routed through the facet and the area of the facet itself. The flow that exits a facet is therefore always larger than the flow that entered it through its sides. The flow accumulates along its path. We call these paths stream tubes which are bounded by two flow lines. In general a stream tube changes its shape from facet to facet which creates variations in the flow density along the stream tube, but also within facets

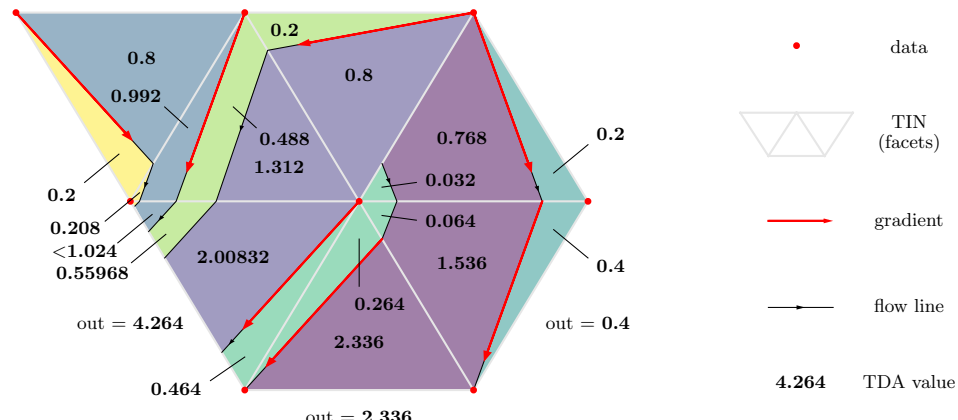


Figure 4. Schematic of a TIN with all stream tubes differentiated in color. For comparison to our FFN estimations (see Fig. 5) the analytical *TDA* values are shown for each stream tube and facet. The value of $TDA < 1.024$ is given by 1.024 minus the very small area of the yellow stream-tube part of that facet. Depending on the structure of the TIN and resulting facet gradients (red arrows), flow lines (black arrow lines) can diverge from each other in diverging landscapes.

(Fig. 4). This is relevant for *SCA* estimation since our flow partitioning assumes a homogeneous flow density along the contours of facets. The error introduced by this assumption occurs only at branching flow facets (Fig. 2), but can propagate downstream (Fig. 5). At branching facets the error is proportional to the *TDA* value, but further downstream the error reduces its relative importance because of additional contributions to the local *TDA*. Furthermore, since *TDA* is preserved and flow partitioning errors are both positive and negative, they will average out in converging landscapes and on larger scales. However, we validate our FFN-derived *SCA* on diverging terrain where the cancellation of errors is suppressed and still observe a better convergence to the analytical solution than the grid-based approach (see Sec. 2.4 and Fig. 9).

In practice, the flow accumulation on the FFN is calculated similar to a breadth-first search along the outgoing links. Starting at facets i , which have no incoming flow (e.g., hill tops and ridges), their outgoing links $i \rightarrow j$ along with the flow they transport f_{ij} [m^2], are added to a First-In-First-Out (FIFO) queue. This queue is successively emptied while the sum $F_j = \sum_{i \in I} f_{ij}$ of all incoming flows for each facet is maintained (I is the set of all facets i that have a link to the current facet j). If the sum F_j [m^2] is complete, the total drainage area draining into the facet j is thereby determined and can,

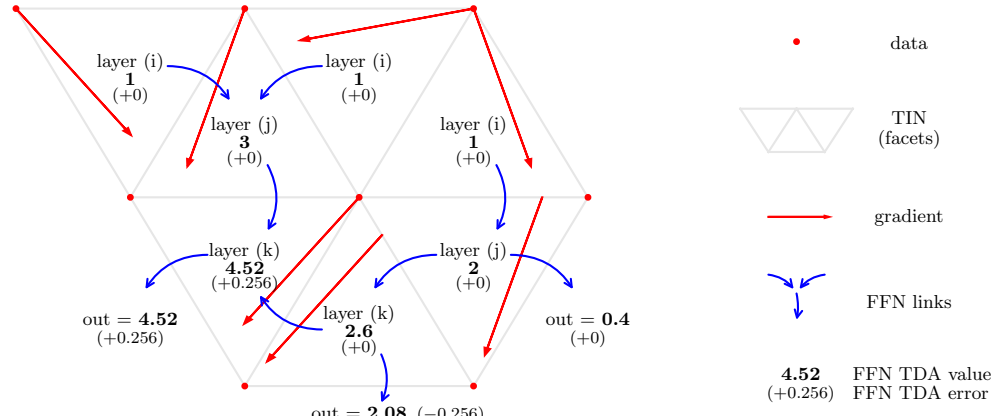


Figure 5. Schematic of the same TIN as in Fig. 4 together with the associated FFN with corresponding layers of the algorithm (i, j, k, \dots). Facets with no incoming links (flow) form the initial layer (i) of the breadth-first walk. Contributions from that initial layer (i) are passed to the next layer (j) and after all contributions are collected from there to the layer (k). The *TDA* value for each facet is shown in bold and its estimation error in parenthesis (cf. Fig. 4).

together with the 2D projected area of the facet j itself (A_j [m^2]), be distributed among its outgoing links. Hence, now the outgoing links of the j -facets, $j \rightarrow k$ along with their outgoing flows f_{jk} , are added to the queue. In this way, the algorithm works itself in layers downhill (i, j, k, \dots) and collects all contributions from all facets (cf. Fig. 5). See the Availability Section for a link to our implementation of this algorithm (Sec. 6) with a pseudo-code description in the Appendix (Sec. A:).

We define the Total Drainage Area (*TDA* [m^2]) of facet j as the sum of all incoming flows F_j [m^2] and its own contribution, the area of the facet A_j [m^2]. Otherwise facets i with no incoming links would have drainage zero. Since facets are planar, contour lines on these are straight and perpendicular to the gradient. Hence, the contour length d_j [m] corresponding to the *TDA* of a facet is the width of that facet projected onto the axis perpendicular to the gradient of the facet. Thus, the FFN-derived *SCA* [m] is defined as

$$SCA_j = \frac{TDA_j}{d_j} = \frac{F_j + A_j}{d_j}. \quad (1)$$

306 2.4 Validation of FFN-derived SCA

307 In order to quantitatively evaluate our flow accumulation scheme, and to compare it
 308 to existing measurements from regularly-spaced data, we consider a Gaussian hill (Fig. 6)
 309 as a synthetic landscape. The Gaussian hill serves as a first approximation of the low
 310 SCA, hilltop-like part of real-world landscapes. We expect point-cloud approaches such
 311 as our FFN approach to be especially useful in divergent parts of the landscape because
 312 the increased point density of point clouds extends studies to smaller SCAs. Note that by
 313 validating SCA we validate TDA and the corresponding contour widths, which are both
 314 independently estimated by our FFN approach. Nevertheless, we are aware of the usefulness
 315 of TDA despite its resolution dependence.

316 Because of the polar symmetry of the surface, the analytical SCA^0 of a Gaussian
 317 hill is one-dimensional in the radius r if polar coordinates (r, ϕ) are used. As for the cone
 318 in *Shelef and Hillel* [2013], or any other hill-like surface with polar symmetry, the TDA
 319 that drains through the circle of radius r and that has the origin at the hilltop, is given by
 320 $TDA(r) = \pi r^2$. Together with the circumference of that circle, which is the corresponding
 321 contour width, the $SCA^0(r)$ at a distance r from the center of such hills is given by

$$322 \quad SCA^0(r) = \frac{r}{2}. \quad (2)$$

323 Note that Eq. 1 is for facets, whereas Eq. 2 is for points on the surface. For a comparison
 324 of the two, we interpret the SCA_j of a facet j as an estimate of SCA at the centroid of the
 325 facet. In this way, we can numerically compare the SCA_j obtained from a facet j to the
 326 corresponding $SCA^0(r_j)$, where r_j is the radial distance of the centroid of facet j .

327 The FFN-derived SCAs are defined for the centroids of the corresponding facets
 328 and are therefore irregularly sampled in space (Fig. 7, dark blue box, top layer). This is
 329 in contrast to established SCA estimates such as D_∞ SCA or MFD SCA which are only
 330 defined for gridded DEMs. To compare our SCA estimates to the existing approaches,
 331 we aggregate the FFN-derived SCAs to a grid (Fig. 7, light blue box, bottom layer) or
 332 we apply the proposed FFN accumulation scheme to the TIN obtained from a gridded
 333 DEM (Fig. 7, green box, bottom layer). These are then compared to the SCAs obtained
 334 by MFD (Fig. 7, red box, bottom layer) and to the SCAs obtained by D_∞ (Fig. 7, orange
 335 box, bottom layer). The D_∞ SCA estimates are shown exclusively in the Supplementary
 336 Material, while here we focus on the MFD results because it performs better than D_∞ on
 337 diverging surfaces [Zhou and Liu, 2002; Erskine et al., 2006].

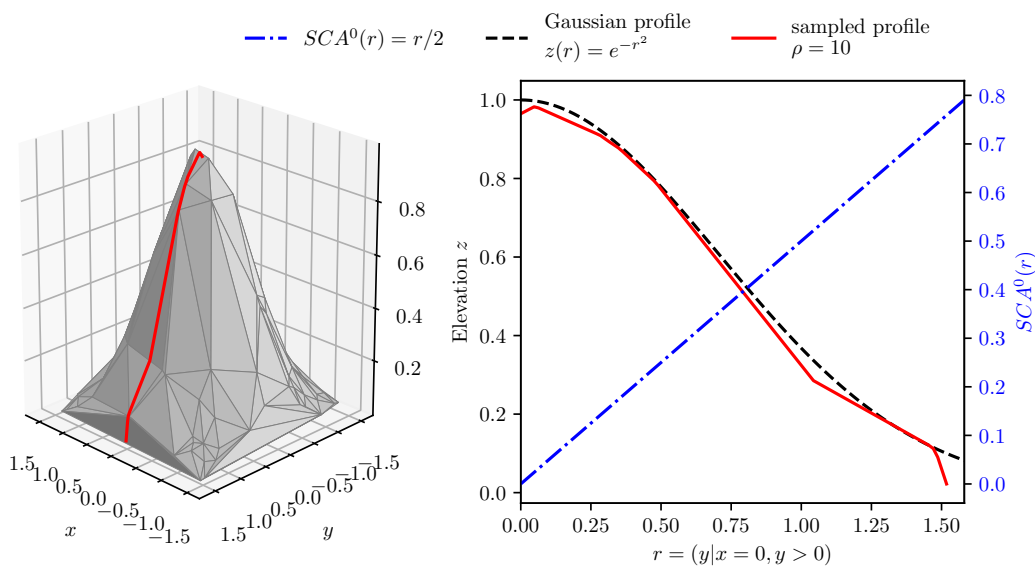


Figure 6. The left-hand side shows a uniform-randomly sampled point cloud of a Gaussian hill with 100 point measurements leading to a point density of $\rho = 10$ number of points per unit area, because the sampled area is ten unit areas. The right-hand side shows the corresponding sampled profile (red solid line) in comparison to the analytical elevation profile (black dashed line) and the analytical solution for SCA (blue dashed-dotted line). See the Supplementary Material Fig. S1 for a sampling with a point density of $\rho = 100$ number of points per unit area.

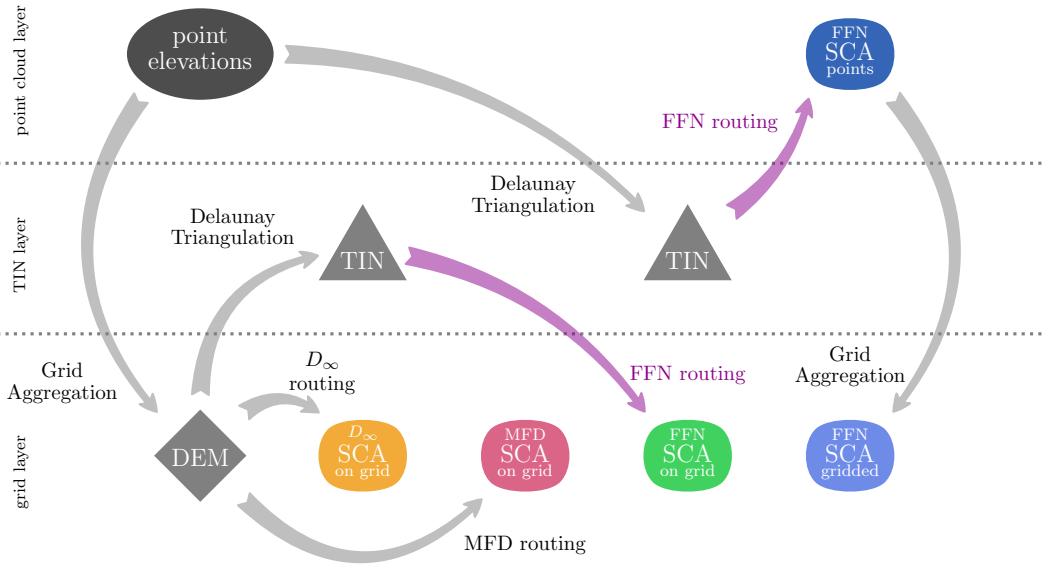


Figure 7. Workflow chart for the different flow accumulation scenarios and the resulting *SCA* estimates.

We separate three layers shown in horizontal order: (i) point-cloud layer, (ii) TIN layer, and (iii) grid layer.

We distinguish between our point-cloud *SCA* estimate in the point-cloud layer from other *SCA* estimates

shown in the grid layer. The color scheme introduced here is consistent with all other following figures of the

manuscript: Blue colors denote FFN flow accumulation performed on point clouds. Dark blue corresponds to

the resulting *SCA* values which are then also structured as a point cloud and light blue corresponds to gridded

versions of those point-cloud *SCA* values. Green colors mark FFN flow accumulation performed on gridded

data. Similarly, red colors denote MFD flow accumulation on gridded data. Note that D_∞ *SCA* estimates

(yellow color) are shown exclusively in the Supplementary Material.

We validate our FFN-derived *SCA* (Eq. 1) in terms of its errors of estimation. Instead of analyzing the root-mean-square errors (RMSEs) as done in earlier studies (e.g., *Shelef and Hillel* [2013], *Qin et al.* [2007], *Zhou and Liu* [2002]), we analyze spatial error patterns in terms of relative deviations from the analytical solution given by

$$\delta SCA(r_j) = \frac{SCA_j - SCA^0(r_j)}{SCA^0(r_j)}. \quad (3)$$

This has the advantage that small deviations in regions of low *SCA* are more visible than similar deviations in regions of high *SCA*. Additionally, since *SCA* varies on many orders of magnitude, and because deviations generally increase with an increase in *SCA*, the RMSE would be dominated by high errors for high *SCA* estimates (see Supplementary Material Fig. S2). Moreover, we do not aggregate deviations into a single value, but rather study the distribution of δSCA estimates.

In particular, we investigate how δSCA varies over different point densities ρ [number of points per unit area] (see Results, Sec. 3.1) and how these are distributed spatially (see Results, Sec. 3.2). For a given ρ , we sample the Gaussian hill on the interval $\sqrt{10}/2 \leq x, y < \sqrt{10}/2$ such that its *xy*-area is 10 square units. In this sampling scheme, a sample with $\rho = 10$ would contain 100 uniformly random distributed elevation measurements from the Gaussian surface (see Fig. 6). Next, for each point density, we sample the hill 1000 times, and therefore obtain a distribution of $1000 \times \rho \times 10$ relative deviations δSCA . We then compare the distribution of δSCA values obtained from the point clouds to three different gridded *SCA* estimation approaches: two obtained from applying MFD routine and FFN routine on the same gridded DEM, and the third obtained by gridding point-cloud FFN-derived *SCAs* to the same grid as the DEM. For the gridded approaches, we compute the DEMs by linear interpolation of the uniform randomly sampled elevation measurements to a grid with the same number of pixels as elevation measurements. Hence, given ρ , we determine the grid cell width w by $w = 1/\sqrt{\rho}$. This procedure of interpolating point measurements to a grid cell elevation is in contrast to directly measuring the surface elevation at the grid-cell centers. However, we consider this to be a more realistic representation of how real-world DEMs are constructed because measurements are not performed at grid cell centers. We perform linear interpolation because it is common and most comparable to TINs.

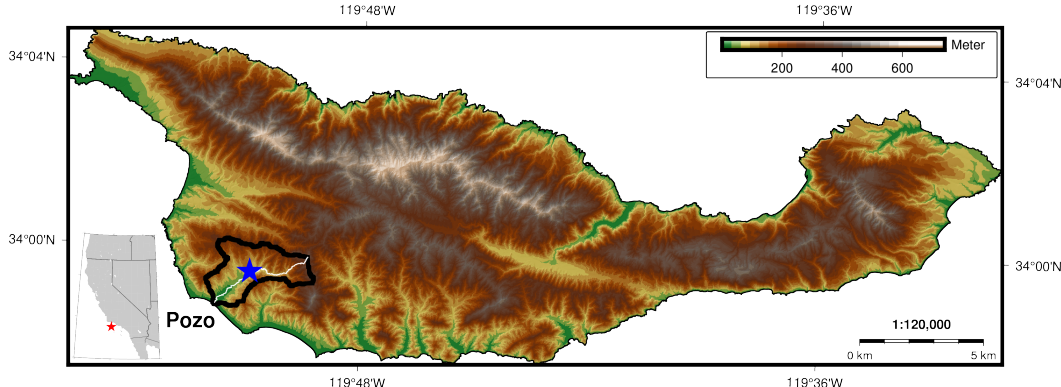
Complementing the above analysis of δSCA distributions and their dependence of ρ , we also analyze the spatial pattern of δSCA which shows how deviations from the an-

385 alytical solution are spatially structured. For this, we choose a specific $\rho = 168.1$ points
 386 per unit area, which results in a point cloud of 1681 uniform-randomly distributed surface
 387 measurements from the Gaussian hill. Correspondingly, we compute a 41×41 pixel DEM
 388 by linear interpolation with a grid-cell width w of $w \approx 0.077$. We compare the following
 389 four scenarios: (i) δSCA from the FFN of the gridded DEM, (ii) δSCA from the FFN of
 390 the point-cloud data, (iii) δSCA by MFD of the gridded DEM as in (i), and (iv) δSCA as
 391 in (ii), but aggregated to the same grid as the DEM.

392 2.5 Application to Lidar point-cloud data

393 Apart from synthetic surfaces, we also apply the FFN approach to airborne lidar
 394 data from the Santa Cruz Island in southern California. This tectonically active, very steep
 395 and densely vegetated terrain provides an ideal location to test the algorithm for an area
 396 where lidar point clouds represent an imperfect characterization of the bare-earth sur-
 397 face [Perroy *et al.*, 2010, 2012; Neely *et al.*, 2017; Baguskas *et al.*, 2014]. In particular,
 398 we choose the Pozo catchment in the southwestern part of the island (see Fig. 8) cover-
 399 ing different lithologies and vegetation covers. In this area, the deeply-incised gullies and
 400 chaparral-like vegetation cover does not always allow for the lidar pulses to reach the sur-
 401 face [Perroy *et al.*, 2010]. We specifically selected this terrain for the difficulties in lidar
 402 point-cloud ground classification, because FFNs can also be constructed from unclassified
 403 or imperfectly classified point clouds.

408 Data were collected using a Riegl LMS-Q560 laser scanner flown on a helicopter
 409 retrieving on average 9 points per square meter leading to a point-cloud data set con-
 410 taining $\approx 7 \cdot 10^7$ points for this catchment [NSF OpenTopography Facility, 2012]. To
 411 ensure accurate triangulation of the data, we apply an initial thinning step that removes
 412 the higher point out of a pair of points if they occur within an xy -distance of less than
 413 5 cm to each other. The xy -distances are computed using the cKDtree implementation
 414 of a quick nearest-neighbor lookup distributed in the spatial module of the scientific
 415 computing package SciPy. This thinning results in a point cloud of $\approx 6 \cdot 10^7$ points with
 416 unique xy -coordinates. Additionally, we use the ground-only classified points in order to
 417 have more comparable results with existing grid-based techniques. The number of ground
 418 points for the Pozo catchment is $\approx 24 \cdot 10^6$.



404 **Figure 8.** Topographic map of the Santa Cruz Island in southern California (cf. red star in inset) with
 405 the Pozo catchment outlined by a black polygon. The white line shows the trace of the longitudinal longest
 406 flow path profile of the application to lidar point-cloud data (Fig. 16). The blue star denotes the center of the
 407 depicted region in the *SCA* pattern analysis (Fig. 12).

419 Lidar data are not randomly distributed: for example, measurements are aligned with
 420 flight lines and higher measurement densities occur for vegetation due to multiple returns
 421 and overlapping swaths. These sampling biases have the potential to bias *SCA* estimates.
 422 In order to partly overcome these biases and quantify *SCA* uncertainties, we propose an
 423 optional bootstrapping approach where we select a subset of k measurements out of N ,
 424 i.e., we cross-validate *SCA* in terms of elevation measurements. Theoretically, the number
 425 of possible bootstrapping samples is finite. However, given an initial number of N mea-
 426 surements and a sample size of k , the number of combinations are give by the binomial
 427 coefficient $\binom{N}{k} = \frac{N!}{k!(N-k)!}$ and therefore in practical terms limitless. For instance, in our
 428 application to lidar point-cloud data of a single catchment on the Santa Cruz Island in
 429 California, we bootstrap our samples from an initial number of $N \approx 6 \cdot 10^7$, or $N \approx 24 \cdot 10^6$
 430 respectively elevation measurements. In a bootstrapping sample, each measurement is cho-
 431 sen with the selection probability P_j^{sel} ,

$$P_j^{sel} = \left(\sum_{i=1}^N \frac{1}{\rho(x_i, y_i)} \right)^{-1} \frac{1}{\rho(x_j, y_j)}, \quad (4)$$

432 where $\rho(x_j, y_j)$ is the spatial point density at (x_j, y_j) . Thus, measurements in regions of
 433 low density ρ are very likely to be chosen, whereas points in densely sampled regions
 434 (e.g., vegetation, overlapping flight lines) are not. This leads to a homogeneous sampling
 435 if not too many measurements per bootstrapping sample are selected. For a homogeneous

sampling the sample size k is limited by $k_{max} < N$, with k_{max} being determined by the lowest spatial densities in the region of interest. However, for our application to lidar data we choose $k = N/2$ as a trade-off between homogeneity and data density. Additionally, we take the Voronoi cell area for each lidar data point as a good approximation for the inverse of the point density. Hence, given the 2D Voronoi tessellation of the region of interest into Voronoi cell areas a_j corresponding to each point measurement at (x_j, y_j) , we approximate the selection probability as,

$$P_j^{sel} = \left(\sum_{i=1}^N a_i \right)^{-1} a_j . \quad (5)$$

According to this probability we select 100 bootstrapping samples with $N/2$ lidar measurements each, from which we obtain an ensemble of 100 FFNs. This results in almost all elevation measurements to be incorporated at least once.

For comparisons to gridded approaches, we generate gridded DEMs from the lidar point cloud samples by linear interpolation as with the synthetic examples, i.e., the number of valid elevation pixels is given by $N/2$. In the Result Section (Sec. 3.3), we compare our FFN approach for lidar data to grid-based approaches in three ways: (i) we compare the distributions of *SCA* for ground-classified points; (ii) we analyze spatial flow patterns and the influence of vegetation and microtopography to such patterns, and compare our FFN approach to MFD in that respect for ground-classified points and the full point cloud; and (iii) since the channel is in parts highly vegetated, we highlight the efficiency of tunnels for the real-world example of tunneling the flow through vegetation and along the channel, and compare longitudinal longest flow path profiles using the unclassified full point cloud.

3 Results

3.1 Dependence of relative deviations on point densities

For the synthetic landscape of the Gaussian hill (Fig. 6) and for our FFN approach on point clouds, relative deviations δSCA decline similar to a power-law $\propto \rho^{1/2}$. We quantify this by the decline of the upper quartile of the δSCA distributions and a corresponding increase of the lower quartile, both towards zero (Fig. 9, dark blue solid lines). Naturally, the convergence of the same *SCA* only aggregated to a grid is very similar (Fig. 9, light blue dashed lines). However, different results are retrieved by flow accumulation on the gridded DEMs of the Gaussian hill. For FFN *SCA* estimations using linear inter-

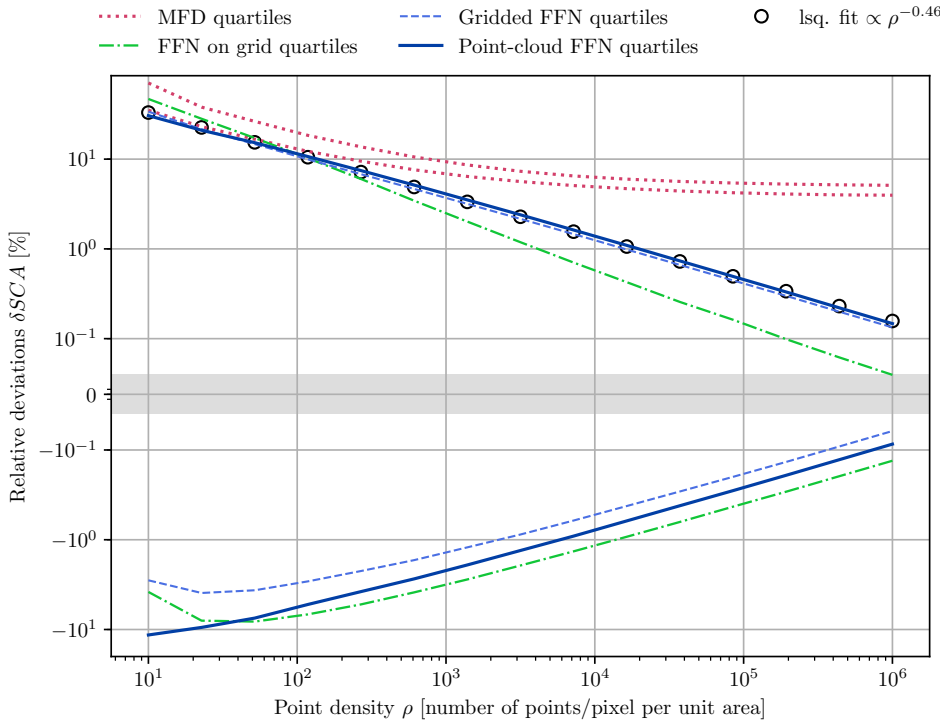


Figure 9. Comparison of relative deviations from the theoretical SCA^0 with numerical SCA estimates of a Gaussian hill for MFD [Freeman, 1991], FFN on gridded DEMs, FFN on the point clouds, and gridded SCA from point-cloud FFNs. The spread of the different error distributions is visualized by the lower and upper quartiles for each point density ρ . Optimal deviations would be 0%. The gridded $SCAs$ from point-cloud FFNs converge similar to the non-gridded $SCAs$ from point-cloud FFNs, whereas the other approaches that route the flow on gridded DEMs suffer from grid effects, i.e., the decline of deviations stagnates or is offset. The gray bar highlights the region of linear y-scale.

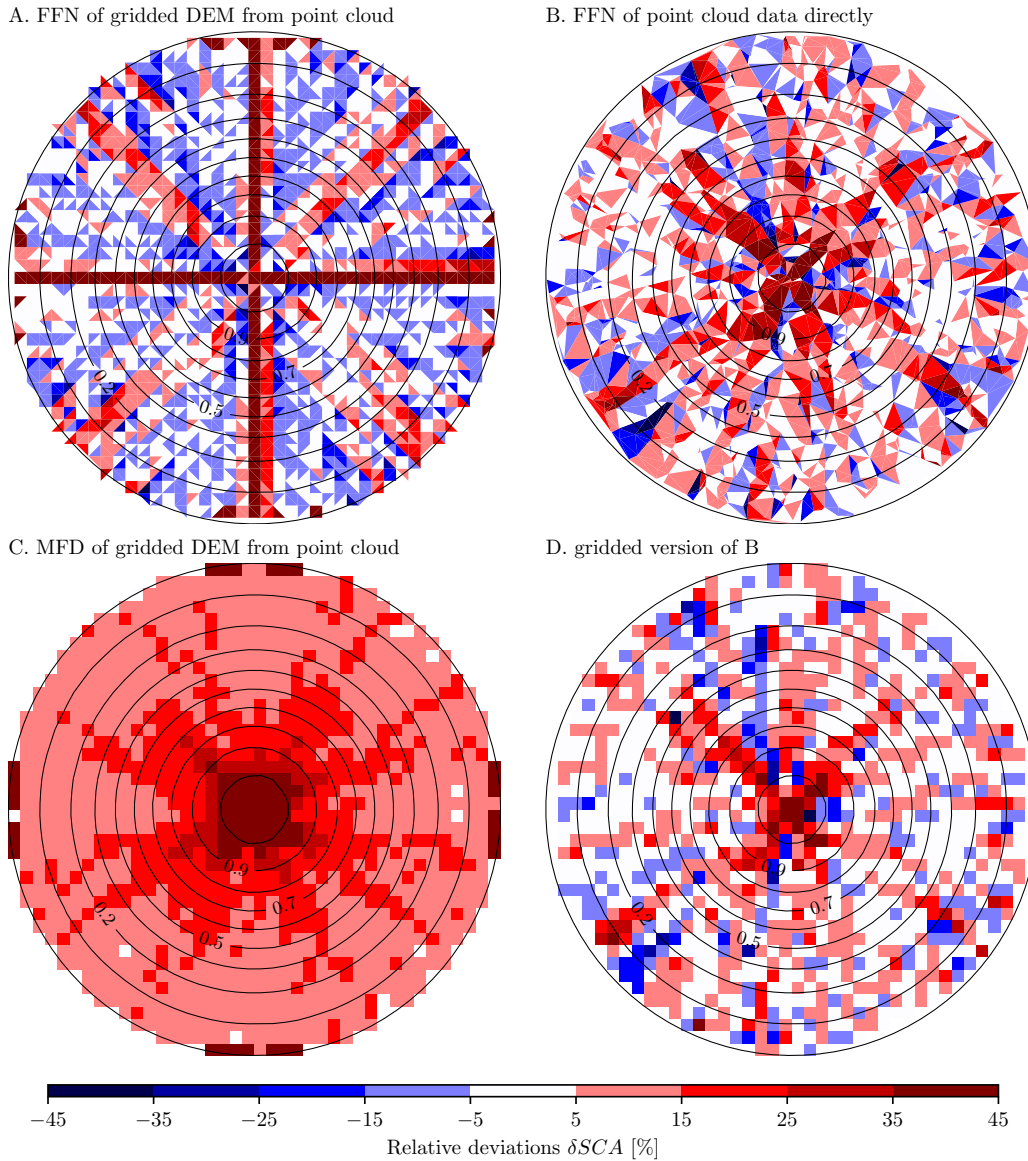
polation DEMs, relative deviations δSCA are larger for low point densities ρ and converge towards zero. However, the lower quartile converges similar to the point-cloud FFN δSCA but offset to larger negative deviations, whereas the upper quartile converges faster (see Fig. 9, green dashed-dotted line). For MFD SCA estimations using linear interpolation DEMs, relative deviations δSCA are larger for low point densities ρ and do not converge towards zero. For overestimations, here represented by both quartiles of the MFD δSCA distributions, the convergence slows down with an increase in ρ until it stagnates at $\delta SCA \approx 5\%$ (see Fig. 9, red dotted line).

481 3.2 Spatial patterns of relative deviations

482 Relative deviations of the point-cloud FFN *SCA* from the Gaussian hill do not ex-
 483 hibit strong spatial patterns except for a radially symmetric increase of *SCA* overestima-
 484 tion close to the center, i.e., with increasing elevation (Fig. 10 B). This holds also for the
 485 gridded version of the same *SCA*, except that some of the smaller deviations from the an-
 486 alytical solution average out with the aggregation to the grid, leading to a larger fraction
 487 of pixels being within the (-5%, 5%) interval (Fig. 10 D). This is in contrast to FFN and
 488 MFD flow accumulation on the gridded DEM (Fig. 10 A, C). As expected from the distri-
 489 butions of δSCA , both show larger deviations from the analytical solution than estimations
 490 directly from point clouds and the largest deviations occur along the cardinal and diagonal
 491 directions, especially for FFN on the gridded DEM. Furthermore, MFD leads more often
 492 to overestimations in *SCA* (Fig. 10 C), whereas FFN approach results in more underesti-
 493 mations (Fig. 10 A).

501 3.3 Pozo catchment lidar point cloud

502 The *SCA* probability density functions (PDFs) estimated by the four different ap-
 503 proaches are fairly similar within their ranges of *SCA* values (Fig. 11 A). All PDFs have a
 504 similarly modulated power law-like tail, which is slightly offset according to the different
 505 normalizations due to different *SCA* value ranges, i.e., different supports. The differences
 506 between the PDFs are highlighted by quantile-quantile plots, which map the quantiles of
 507 our proposed point-cloud FFN *SCA* measure to the corresponding quantiles of the three
 508 compared approaches (Fig. 11 B). Since the point-cloud FFN *SCA* has the largest value
 509 range, ranges of very low (high) quantiles of the point-cloud FFN *SCA* correspond to
 510 the minimum (maximum) of the other SCAs. Within the possible range of *SCA* values,
 511 quantile-quantile plots have a finite positive slope. If two PDFs are identical up to a nor-
 512 malization constant, their quantile-quantile function will have a slope of one. None of the
 513 compared PDFs are identical in that sense and consequently their quantile-quantile func-
 514 tion slopes vary around one. This variation is most pronounced for MFD *SCA*, less for
 515 FFN on grid *SCA* and gridded FFN *SCA*. Note that the variation of slopes is very similar
 516 between these three quantile-quantile functions for intermediate *SCA* values (from ca. 10^1
 517 to 10^5), especially between the three FFN approaches.



494 **Figure 10.** Comparison of three different FFN approaches and MFD [Freeman, 1991] in respect to δSCA
495 patterns. All four scenarios rely on the same set S of 1681 uniform random surface measurements from the
496 same Gaussian hill as in Fig. 9: A. S aggregated to a 41×14 grid DEM with the same number of measure-
497 ments as grid cells ($\rho = 168.1$ number of points per unit area) and δSCA is of the FFN of that DEM. B.
498 δSCA from the FFN of S directly. D. Gridded SCA from the same FFN as in B, and C. SCA via MFD from the same
499 underlying gridded DEM as in A. Black contour lines indicate unit-less elevation contours of the Gaussian hill
(0 – 1).

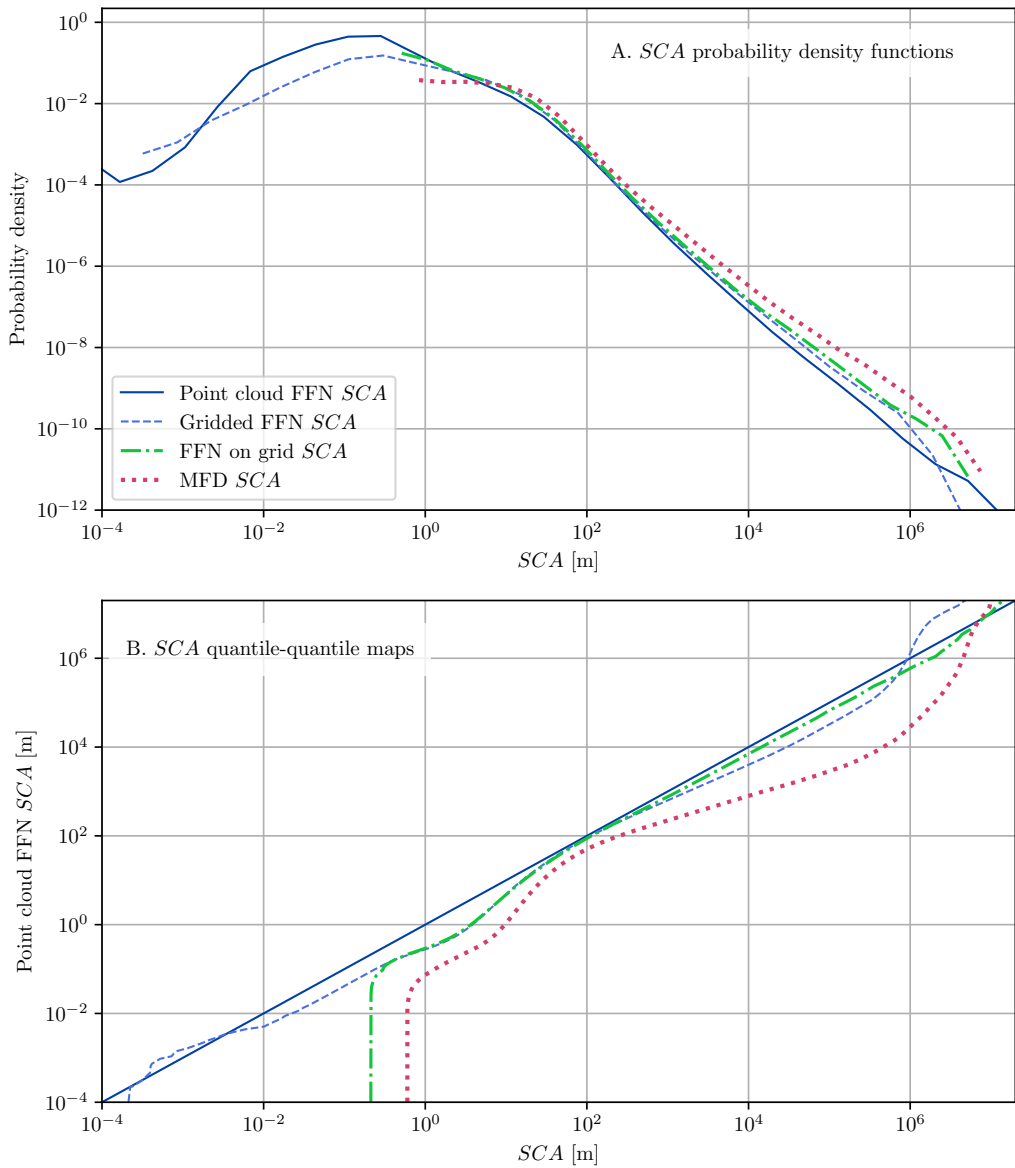
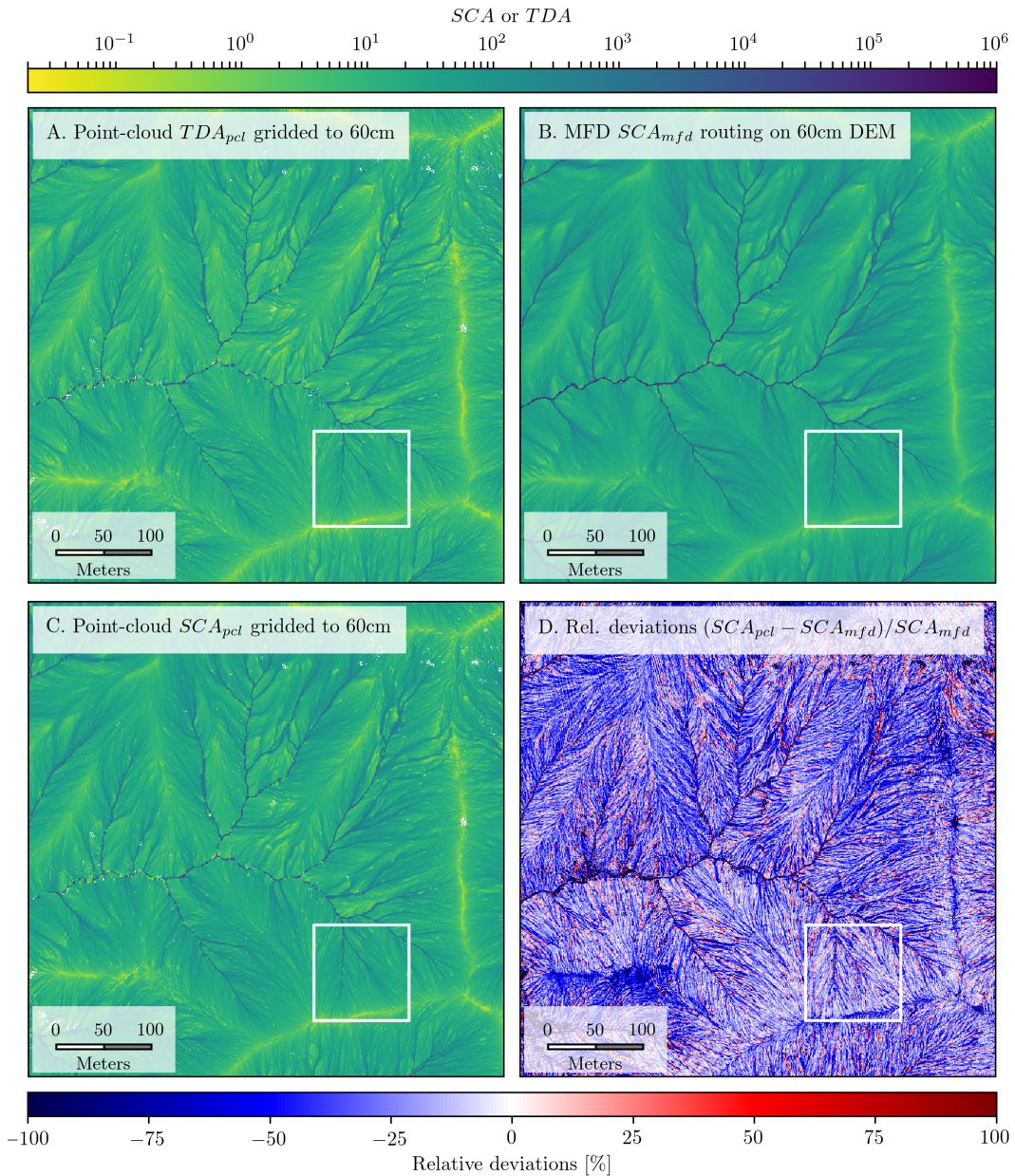


Figure 11. A. Probability density function estimates for SCA of the entire Pozo catchment. B. Quantile-quantile maps corresponding to (A) for quantile comparisons to the point-cloud FFN SCA. The flow accumulations from the 60 cm DEM ensemble (FFN on grid and MFD) fail to resolve the roll-over at ≈ 10 cm due to the too coarse resolution. The gridded point-cloud SCA density depicts the roll-over less pronounced and washed out compared to the point-cloud FFN SCA. For the common range of larger SCA values, densities are in good agreement, with differences being mostly explainable by grid effects.

The spatial *SCA* patterns obtained from the MFD routine on the 60 cm DEM ensemble (Fig. 12B) contain no *SCA* values below 0.36 due to the limit in spatial resolution. Our point-cloud estimates of *TDA* and *SCA* however, although gridded to the same resolution, are computed directly from irregular data and resolve smaller drainage areas (Fig. 12A, C). The overall flow pattern in terms of the shapes of the rivers and the magnitudes of the *SCA* values are similar for both SCA_{pcl} and SCA_{mfd} . However, relative deviations between both reveal pronounced differences in channels and at hill tops (Fig. 12D). Despite many positive deviations (red), most deviations are negative (blue), i.e., SCA_{pcl} is often lower than SCA_{mfd} . This is especially visible at broad hilltops and at channel boundaries (cf. Fig. 13). Possible influences of vegetation are best seen in combination with the point-cloud intensity which is low for vegetated points (Fig. 14). Focusing on two arbitrary starting points of flow lines, we compute for each FFN of the bootstrap ensemble one deterministic FFN flow line for each starting point. This provides us with an ensemble of FFN flow lines for each starting point that captures the flow-line uncertainty given the point-cloud elevation data. With individual flow lines depicted, a tunnel is exemplified by a long straight part in the flow line. These occur mainly within vegetated regions, especially if the full unclassified point cloud is studied (Fig. 15). However, FFN flow lines rather meander around some vegetated parts or get dispersed (Fig. 14B).

The longitudinal flow path profiles for the FFN *SCA* of the unclassified full point cloud and the MFD *SCA* of the longest flow path in the catchment are estimated in terms of the path distance from the hilltop (Fig. 16). The two profiles are quite similar for low path distances, but are visibly offset for the rather steep descent around 750 m to 1000 m. In the detailed views of the profiles from the hilltop (Fig. 16 A) and the vegetated channel (Fig. 16 B), the interquartile range (IQR, gray shaded regions) of the surrounding elevations, i.e., < 1 m from the channel, are better resolved. For vegetated regions, this distribution is shifted towards higher elevations and the flow is routed via tunnel (a few representative examples of which are shown using magenta lines). Particularly for MFD, we observe flat sections which correspond to regions which have undergone sink-filling. The point-cloud FFN *SCA* increases on average monotonically as elevation decreases, but shows fluctuations on smaller length scales due to branching and merging of the channels.



543 **Figure 12.** Map view comparison of our TDA and SCA point-cloud estimates with the MFD SCA on 60 cm
 544 DEM resolution of the Pozo catchment in the southwestern part of the Santa Cruz Island, California (see blue
 545 star in Fig. 8). In the left column our point-cloud estimates TDA_{pcl} (A) and SCA_{pcl} (C) gridded to 60 cm
 546 using the ground-classified points only. In the right column for comparison the mean MFD estimate of SCA
 547 (B) using the 60 cm DEM ensemble, i.e., $SCA_{mfd} \propto TDA_{mfd}$, and the relative deviations of our SCA_{pcl} to
 548 SCA_{mfd} in percent (D). The outlined insets are shown in Fig. 13, 14 and 15.

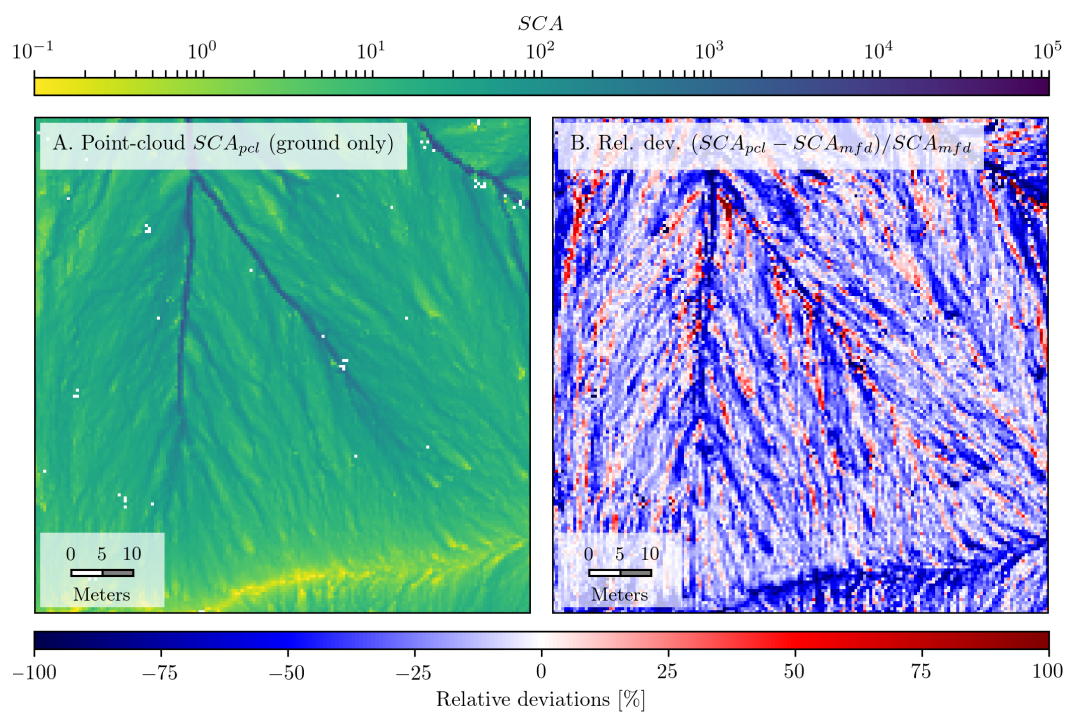
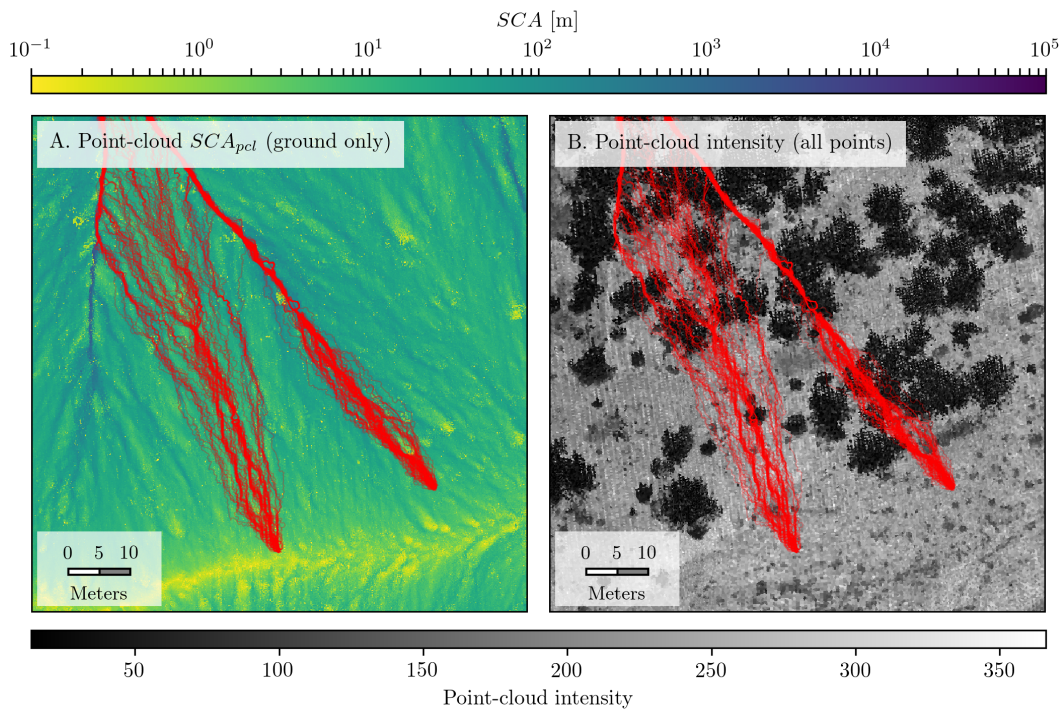
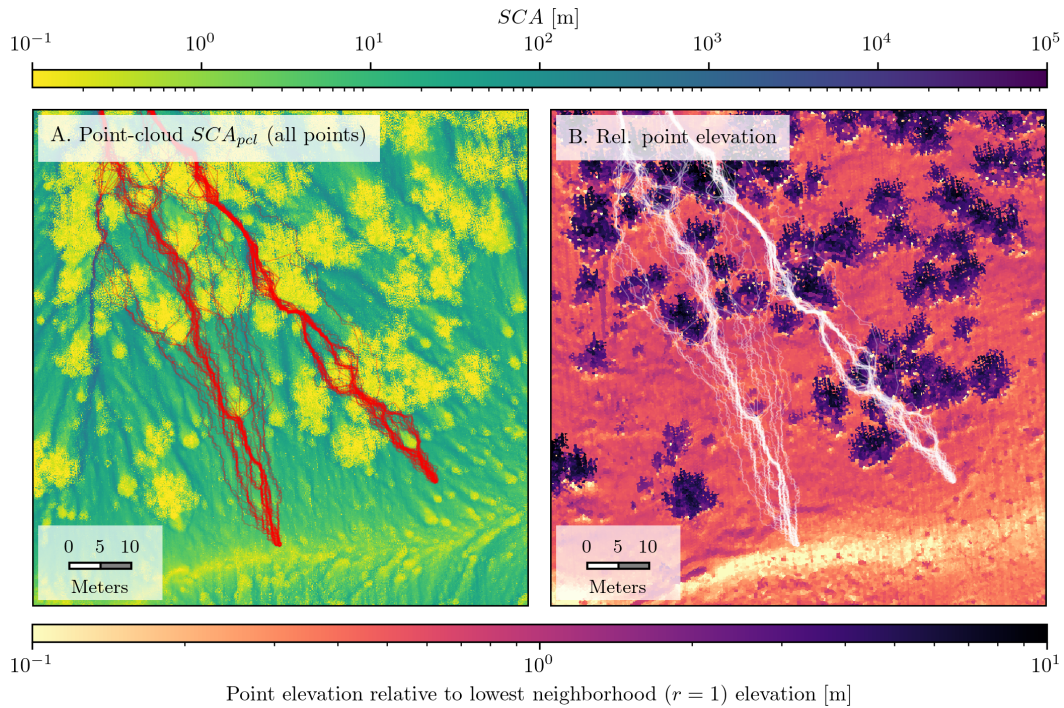


Figure 13. Corresponding to the inset of Fig. 12 the map view of our mean SCA_{pcl} (A) and its relative deviations (B) to mean SCA_{mfd} from the 60 cm DEM ensemble. Blue deviations, for instance at the hill top, are due to MFD's tendency to overestimate SCA in diverging parts of the landscape. Red deviations emerge as additional small-scale channels in the SCA_{pcl} compared to the SCA_{mfd} field.



553 **Figure 14.** Corresponding to the inset of Fig. 12 the map view of SCA_{pcl} (A) in comparison to the point-
554 cloud intensity (B), revealing subtle influences of chaparral vegetation (slightly darker intensity). The spatial
555 sub-sampling approach allows for an ensemble of flow lines (red lines) for each starting point although each
556 individual FFN flow line is deterministic. Shown are two examples close to the hilltop. Both ensembles are
557 for the ground-classified points.



558 **Figure 15.** Corresponding to the inset of Fig. 12 the map view of the unclassified SCA_{pcl} (A) in comparison
559 to vegetation height (B), highlighting influences of vegetation points to flow line ensembles. The spatial
560 sub-sampling approach allows for an ensemble of flow lines (red lines in A and white lines in B) for each
561 starting point although each individual FFN flow line is deterministic. Shown are two examples close to the
562 hilltop. Both ensembles are for the unclassified full point cloud.

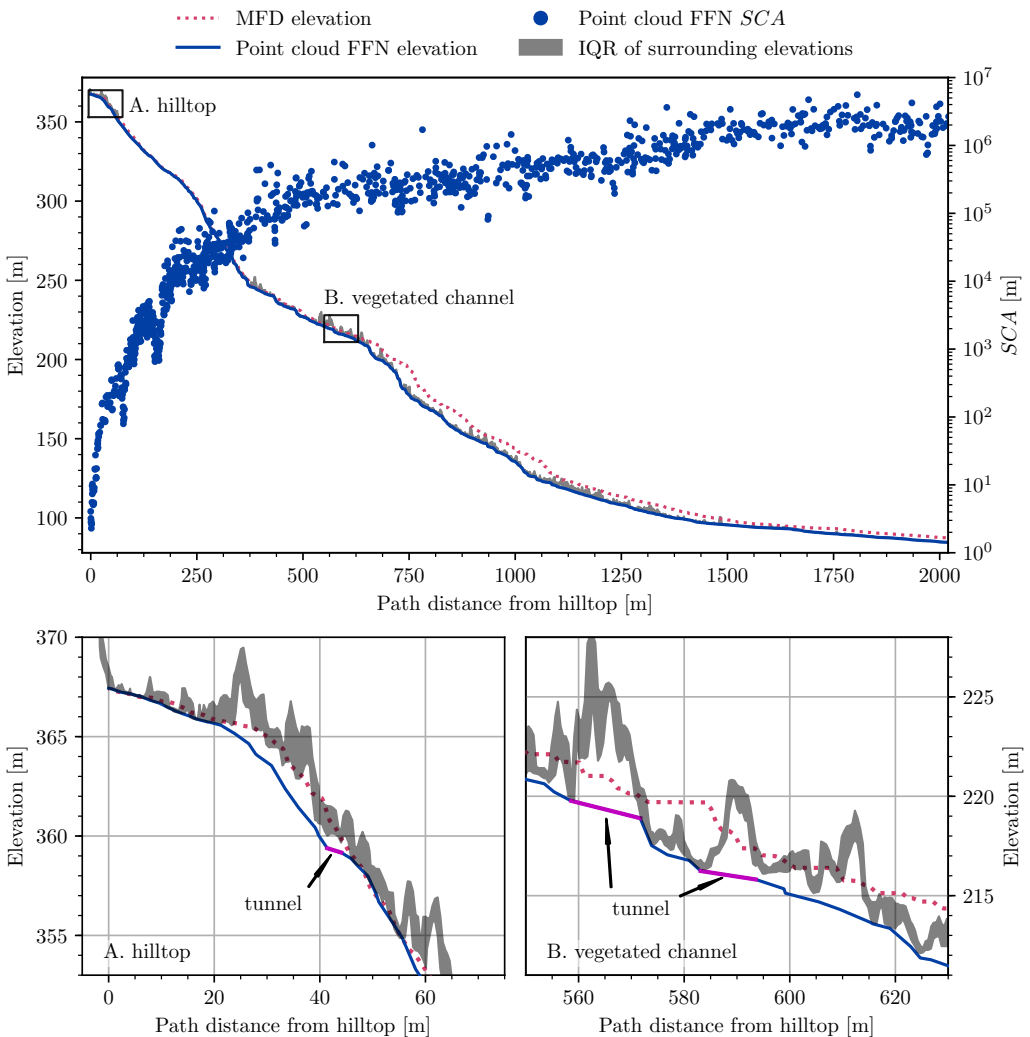


Figure 16. Longitudinal flow path profile for the longest flow path of the Pozo catchment on the Santa Cruz Island (see white trace in Fig. 8). Each point marker of the profile *SCA* corresponds to a node from the FFN of the point-cloud data including vegetation (from one bootstrap sample). The interquartile range (IQR) of all elevations surrounding the path of the profile within a 1 m radius is shown in gray. Vegetation in the point-cloud data leads to high IQR relative to the bare-earth elevation. Links of the point-cloud FFN then tunnel through vegetation and become longer (cf. insets A, B with three tunnels being highlighted in magenta). For comparison the corresponding MFD profile is shown (red dotted curve). Even though the MFD flow path tracing was performed on an approximately vegetation free DEM, DEMs are constructed from ground-classified points only, the sink-filling leads to an in parts step-wise profile (see inset B of the vegetated channel). Additionally, the MFD flow has a more meandering path than the FFN flow, which leads to a shift of the MFD profile towards longer path distances.

586 4 Discussion

587 4.1 Dependence of relative deviations on point densities

588 Our results suggest that relative deviations δSCA for flow accumulation on DEMs
 589 from linearly interpolated point clouds are less centered around optimal deviations ($\delta SCA =$
 590 0) than for flow accumulation on the point clouds assuming the same linear model of a
 591 TIN. Although FFN on grid δSCA distributions converge similarly to point-cloud FFN
 592 δSCA distributions, they are biased by underestimations due to grid effects. MFD δSCA
 593 distributions on the other hand have higher quartiles due to *SCA* overestimations. Regarding
 594 MFD convergence, we note that for point densities between 10^1 to 10^2 points or pixels
 595 per unit area, the convergence is comparable the FFN, for ρ between 10^2 to 10^4 the con-
 596 vergence slows down, and from 10^4 points per unit area on, an increase in spatial resolu-
 597 tion has no effect on MFD *SCA* accuracy, i.e., it stays at a fixed overestimation of $\approx 5\%$.
 598 However, for the FFN flow accumulation on the point clouds, relative deviations steadily
 599 decline by one order of magnitude for an increase in point density by roughly two orders
 600 of magnitude. For an analysis regarding the scaling in computational costs we refer to the
 601 Supplementary Material (see Fig. S5, S6).

602 4.2 Spatial patterns of relative deviations

603 The analysis of spatial patterns of δSCA illustrates the advantage of deriving *SCA*
 604 from irregular point clouds instead of first gridding the data and then deriving flow accu-
 605 mulations. The gain in *SCA* precision is not due to more elevation measurements in the
 606 point cloud versus pixels in the DEM, both are kept equal, but due to a lack of grid ef-
 607 fects. For the example of a 41×41 grid and $\rho = 168.1$ number of points per unit area,
 608 we have on average one surface measurements per grid cell (Fig. 10). Apart from the vari-
 609 ability in *SCA* accuracy due to random sampling, *SCA* tends to be overestimated close to
 610 the hill top for all four scenarios. However, since we study relative deviations, errors close
 611 to the hill top are emphasized, i.e., $\delta SCA \rightarrow \infty$ as $r \rightarrow 0$.

612 Another spatial pattern is aligned with the orientation of the grid and best visible in
 613 the first scenario (i) of FFN *SCA* estimation from the gridded DEM (Fig. 10A). For this
 614 case, *SCA* is highly overestimated along the cardinal directions of the grid and rather un-
 615 derestimated otherwise. Such spatial patterns in relative deviations are also caused by grid
 616 effects. For MFD *SCA*, grid effects are more difficult to see at this coarse resolution, but

these become more pronounced at higher resolutions and grids with perfect elevation data or other flow accumulation algorithms such as D_∞ (see Supplementary Material, Fig. S3, S4).

4.3 Implications of grid effects and SCA

DEM metrics such as TDA , SCA , slopes, curvatures, etc., are typically calculated using the gridded product, rather than using the TIN of measured data directly. Here we put forward the idea, of taking advantage of the usually much higher resolution of the raw measurements instead of aggregating measurements to a grid. For our examples we choose grids with on average one measurement per grid cell, however that is not often the case. The motivation to take point-cloud data directly is twofold: First, the above analysis illustrated the benefits in accuracy of higher measurement densities (cf. Fig. 9). Second, the regularity of grids can cause spatial effects that propagate on scales beyond the spatial scale of grids (cf. Fig. 10). Any neighborhood-based flow accumulation will suffer from the fact that locally only a finite set of flow directions occur. Extreme cases are the $D4$ and $D8$ flow directions, but even D_∞ and MFD allow only the four cardinal directions plus the four $\pi/4$ -shifted directions [Tarboton, 1997; Freeman, 1991]. Because these routines are designed for square grids only, the eight local flow directions are also globally the only ones occurring. Biases due to imperfect flow partitioning can therefore aggregate along these directions together with the flow aggregation. On cones, or other highly symmetric surfaces, these biases create especially obvious and well known artifacts in the flow as previously described by Shelef and Hillel [2013], Qin et al. [2007], Zhou and Liu [2002] and Freeman [1991]. In order to minimize such grid effects, the MFD algorithm includes an additional parameter that is adjusted to the analytical solution of the SCA of a cone [Freeman, 1991]. However, although this leads to reduced grid effects when compared to D_∞ , they are still apparent (cf. Fig. S4, S5). In contrast, on irregular sampled data a finite-neighborhood flow accumulation scheme does not lead to a finite set of total flow directions. This is an advantage of our FFN approach, as it is explicitly designed for irregular sampled data such as point clouds. Sometimes an aggregation of measurements to a grid might seem inevitable because of noisy data or the necessity of a gridded flow product for further analysis, but in order to avoid grid effects it is advisable to aggregate SCA results instead of elevation measurements.

648 4.4 Pozo catchment lidar point cloud

649 Due to the high spatial resolution of the airborne lidar point cloud, and especially
 650 due to the random homogeneous density sampling, we have a larger ensemble of *SCA*
 651 estimates for the point-cloud data as well as for the grid-based approaches.

652 The ensembles of *SCA* values allow a smooth and reliable histogram estimation,
 653 even for very small drainage areas (Fig. 11 A, solid dark-blue line). If this ensemble of
 654 point-cloud *SCA* estimates is aggregated to the 60 cm grid prior to the density estima-
 655 tion, the correspondingly estimated probability density function (PDF) is flattened out, i.e.,
 656 grid cells with many low *SCA* estimates (e.g., from vegetation or boulders) and relatively
 657 fewer, but much higher *SCA* estimates (e.g., from channels or river basins) will aggre-
 58 gate to grid cells of high *SCA*. Although this is intended, because grid cells should repre-
 659 sent the channel *SCA* if they include a channel, it leads to relatively fewer low *SCA* and
 660 higher *SCA* values (Fig. 11 A, dashed light-blue line). Essentially this is due to the too
 661 coarse grid resolution of 60 cm. The same holds for MFD and FFN on the 60 cm DEM
 662 ensembles, but for a different reason. For flow accumulation on grids, channels have a dis-
 663 cretized width of multiples of the grid resolution. This leads to an over representation of
 664 channels in the PDF of *SCA* estimates (see also Fig. S6 for results corresponding to D_{∞}).
 665 Less so for the FFN on the gridded DEM, because the grid is triangulated and the flow
 666 is discretized by triangles with an area of half a grid cell. This is also the reason why
 667 FFN flow accumulation on the 60 cm DEM resolves *SCAs* below 0.36 cm (cf. Fig. 11 A,
 668 dashed-dotted green line). The smallest *TDA* in this case is 0.18 m^2 and the smallest *SCA*
 669 is therefore $0.6\sqrt{2}/4 \text{ m}$.

670 The quantile-quantile maps for the *SCA* PDFs highlight the differences between
 671 our point-cloud *SCA* estimate and the other grid-based approaches in terms of quantile-
 672 position thresholds (Fig. 11 B). Since all PDF estimates have a different support, the im-
 673 ages of the quantile-quantile maps vary between densities. In that sense, absolute differ-
 674 ences between probabilities are meaningless because each PDF is normalized on its own
 675 support. The more parallel a density relative to the reference line of the point-cloud *SCA*
 676 PDF is (Fig. 11 B, solid dark-blue line), the more similar their quantiles vary with *SCA*.
 677 For instance, on the interval $10^{-2} \leq \text{SCA} < 10^6$ the PDF for the gridded *SCA* evolves
 678 more parallel to the PDF for the point-cloud *SCA* than the PDFs for the flow accumula-

679
tion on the gridded DEMs. Overall, the FFN-based PDFs are more parallel to the refer-
680
ence PDF than the MFD PDF.

681
In an analysis of spatial *SCA* patterns, we confirm the aforementioned differences in
682
SCA for the different approaches and the dependence of these differences on *SCA* magni-
683
tude (Fig. 12). In contrast to low *SCA* values from the point-cloud FFN, low MFD *SCA*
684
values are bounded by the resolution of the DEM and cannot resolve areas smaller than
685
0.36. This effect is further emphasized by the tendency of MFD to overestimate *SCA* val-
686
ues (Fig. 9). For the comparison by relative deviations (Fig. 12D and 13B) this results in
687
negative deviations (blue) for regions where SCA_{mfd} is limited by the resolution of the
688
DEM. Interestingly, our SCA_{pcl} reveals channelization closer to the drainage divide than
689
 SCA_{mfd} , which leads to positive deviations (red) in the form of channels (Fig. 13).

690
Further, it is possible to see feedbacks between vegetation and channelization using
691
this high spatial resolution lidar data. Due to the stabilization of soil by vegetation [Lud-
692
wig *et al.*, 2005], soil is rather eroded around it, leading to more surface runoff there than
693
in vegetated patches. This enhances erosion around vegetation and combined with weak
694
lithologies leads to early channelization close to the drainage divide [Perroy *et al.*, 2012].
695
Additionally, vegetation traps fluvial and aeolian sediment which elevates vegetated patches.
696
However, since we use only ground classified points, vegetated patches are gaps in the
697
point cloud that are incorporated into the FFN by gap-spanning facets. In order to see
698
the influence of these gaps we compare our flow-line ensemble using only ground points
699
(Fig. 14) with an ensemble using all points (Fig. 15). Both ensembles show a very similar
700
SCA as well as flow-line pattern with the ground-only ensemble being less influenced by
701
vegetation. In the flow-line ensemble using all points vegetation acts as stable patches, and
702
forces flow around vegetation rather than through itself. Most flow lines go around bushes
703
and trees with only few tunnels going through bigger vegetation patches. The biggest dif-
704
ference between the ensemble using only ground-classified points and the ensemble using
705
all points is seen for high vegetation (dark colors in Fig. 14.B and 15B). For the unclassi-
706
fied point-cloud ensemble flow lines rather meander around high vegetation such as trees,
707
whereas for the ground-points ensemble flow lines are less obstructed. This suggests that
708
the erosional imprint of trees is overestimated in the unclassified point cloud. Neverthe-
709
less, both ensembles show meandering around chaparral vegetation with early channeliza-
710
tion close to the drainage divide.

The efficiency of tunnels in our FFN approach is also demonstrated with a comparison of two longitudinal flow path profiles: one for our point-cloud FFN approach and the other from the SCA_{mfd} field of the approximately vegetation-free gridded DEM ensemble (Fig. 16). Especially within the first kilometer from the hill top, there are very steep and highly vegetated parts of the channel where lidar pulses do not reach the surface. As a result, some of the grid cell elevations are over estimated and combined with the discretization of the channel into grid cells, this leads to sinks in the channel. Resolving these by a sink-filling approach leads to plateaus (i.e. flat sections) in the MFD profile, while in the FFN profile sinks are circumvented by tunneling (cf. Fig. 16 A, B). Although the tunnels are often much longer than the grid cell spacing for MFD, the resulting FFN profile appears to be more smooth. In map view, this also leads to a straighter and less meandering path for the FFN profile. The MFD profile in turn is shifted to the right of the FFN as a result. Since the spatial resolution of the point cloud samples is the same than that of the gridded DEMs, this suggests that discretization of the channel into a series of grid cells makes the river longer than it actually is (cf. Fisher *et al.* [2013]). This highlights again the advantage of irregular point-cloud sampling. Even though the FFN longitudinal flow path profile includes many tunnels due to vegetation, it records the channel bottom at those geographic locations where the corresponding elevations were measured and not at predefined grid cell centers.

4.5 Outlook: additional FFN-based metrics

Drainage area is only one measure of interest in flow terrain analyses, and it is often accompanied by measures such as direction of descent, slope, and curvature. Although an analysis of these is beyond the scope of this study, some of them are directly retrievable by our FFN approach. For instance the direction of descent and slope at each facet would be given by the gradient of that facet. An alternative to the slope could be the derivative of elevation along FFN flow lines and similar to that the second derivative could serve as a curvature estimate.

5 Conclusions

We presented a novel approach for the representation of flow on topographic surfaces and the estimation of SCA on irregular sampled elevation measurements. The approach is based on the calculation of a Triangulated Irregular Network (TIN) of measured

742 data by Delaunay triangulation and routes the flow from each facet of the TIN according
743 to the so called Facet-Flow Network (FFN). The validity of the linear TIN model depends
744 on the data density and surface roughness. Considering the analyses done in this study
745 we conclude that a TIN is a sufficient surface model for high resolution data such as air-
746 borne lidar point clouds. Based on the FFN, we also present a fundamentally different
747 treatment of sinks without any modification of the digital representation of the landscape,
748 i.e., changing elevation measurements by sink filling or carving. This also allows a quan-
749 tification of uncertainties in *SCA* and resulting flow patterns by generating a bootstrapping
750 ensemble of elevation measurements and therefore an ensemble of FFNs. Both, the treat-
751 ment of sinks as well as the bootstrap sampling are optional steps, but useful in real-world
752 applications. Results from our FFN point-cloud approach were compared to grid-based
753 procedures for the estimation of *SCA* using real-world data as well as synthetic data from
754 a Gaussian hill where the analytical solution for *SCA* is known. For all comparisons we
755 use Digital Elevation Models (DEMs) that have the same number of pixels as elevation
756 measurements in the corresponding point clouds. Based on these comparisons, we con-
757 clude that our network-based approach generates flow patterns closer to the analytical so-
758 lution on a synthetic surface than for example the MFD flow accumulation and offers the
759 following advantages: (i) The association of a well defined contour width to each link of
760 the FFN, which grants an accurate estimation of *SCA* from the corresponding *TDA* val-
761 ues; (ii) The applicability to irregular spaced data makes high-resolution point-cloud data
762 directly accessible to flow path tracing, not requiring the creation of DEMs. (iii) Addition-
763 ally, this allows for a dynamic data density in terms of a varying point density depending
on, for instance, surface roughness or measuring technique.

765 Although in this study we create high-resolution DEMs with the same number of
766 pixels as points in the point cloud, this is only for comparison and not a recommended
767 DEM creation scheme. Typical DEMs have less pixels than the underlying point cloud in
768 order to mitigate elevation uncertainties and to avoid interpolation artifacts. Compared to
769 that, our FFN approach is beneficial regarding an increased *SCA* accuracy due to a more
770 dense spatial sampling, but it also makes it possible to study features in the landscape that
771 are smaller than the grid cell width of such typical DEMs.

772 6 Software availability

773 A Python module written in C called *FacetFlowNetwork*, which implements the FFN
construction and *SCA* estimation, is available at [https://github.com/UP-RS-ESP/
774 FacetFlowNetwork](https://github.com/UP-RS-ESP/FacetFlowNetwork). Additionally, an implementation of the MFD algorithm by *Freeman*
775 [1991], based on the implementation of *Pelletier* [2012], is available at [https://github.
776 com/UP-RS-ESP/mfdrouting](https://github.com/UP-RS-ESP/mfdrouting).

777 Acknowledgments

778 Bedartha Goswami was funded by a scholarship from the Ministry of Science and Education
779 of the state of Brandenburg (MWFK).

780 We thank six anonymous reviewers for the careful reading of the manuscript and
781 their detailed and constructive reviews.

783 A: FFN flow accumulation algorithm

784 Our flow accumulation algorithm requires the in-degree K_j of each facet j in the
 785 FFN in order to confirm the arrival of all in-flows. We compute the in-degree by sim-
 786 ple counting with two nested for loops (cf. Alg. 1). This is reasonably fast because facets
 787 have either one or two out-going links, i.e., the outer loop has N (number of facets) itera-
 788 tion and the inner only one or two.

789 Similar to the array of in-degrees K , the flow accumulation algorithm maintains an
 790 array of counters $Seen$ and an array for the sums of in-flows F . These arrays are initial-
 791 ized as zero vectors (Alg. 2, L1). The sum of in-flows F_j for a given facet j together with
 792 the area A_j of the facet is defined as its TDA_j (cf. Eq. 1).

793 The breadth-first walk starts at facets i that have no in-degree ($K_i == 0$, Alg. 2,
 794 L2) and initializes a queue with their down-hill neighbors j along with the flow f_{ij} from
 795 i to j . This queue is emptied in a while loop while the counters $Seen$ and the sums of in-
 796 flows F are updated (Alg. 2, L5 and L6). If the counter $Seen_j$ for a given facet j is equal
 797 to its in-degree ($Seen_j == K_j$, Alg. 2, L7), all in-flows are accumulated and are passed on
 798 to the next layer of k -facets.

799 If the facet j is a sequential or merging facet, a_{jk} and w_{jk} are given by $a_{jk} = A_j$
 800 and $w_{jk} = 1$, because there is only one down-hill neighbor k . However, if the facet j is a
 801 branching facet the areas a_{jk} are given by the areas of two corresponding sequential facets
 802 and the weights w_{jk} are given by l_{left}/l_{orig} and l_{right}/l_{orig} respectively (cf. Fig. 2).

Algorithm 1 compute in-degree K for all facets

```

1:  $K \leftarrow \vec{0}$ 
2: for all facets  $i$  do
3:   for all down-hill neighbors  $j$  of facet  $i$  do
4:      $K_j = K_j + 1$ 
5:   end for
6: end for
```

Algorithm 2 flow accumulation by a breadth-first search on the FFN

```
1: Seen and  $F \leftarrow \vec{0}$ 
2: Queue  $\leftarrow$  all down-hill neighbors  $j$  of facet  $i$  with  $K_i == 0$  and corresponding  $f_{ij}$ 
3: while Queue is not empty do
4:    $j$  and  $f_{ij} \leftarrow$  facet and flow from Queue
5:    $F_j = F_j + f_{ij}$ 
6:    $Seen_j = Seen_j + 1$ 
7:   if  $Seen_j == K_j$  then
8:     for all down-hill neighbors  $k$  of facet  $j$  do
9:        $a_{jk} \leftarrow$  area  $A_j$  of facet  $j$  that drains into  $k$ 
10:       $f_{jk} \leftarrow a_{jk} + w_{jk} \cdot F_j$ 
11:       $k$  and  $f_{jk} \rightarrow$  Queue
12:    end for
13:  end if
14: end while
```

803 **References**

- 804 Arrowsmith, J. R., and O. Zielke (2009), Tectonic geomorphology of the San Andreas
805 Fault zone from high resolution topography: an example from the Cholame segment,
806 *Geomorphology*, 113(1), 70–81.
- 807 Baguskas, S. A., S. H. Peterson, B. Bookhagen, and C. J. Still (2014), Evaluating spa-
808 tial patterns of drought-induced tree mortality in a coastal California pine forest, *Forest
809 Ecology and Management*, 315(C), 43–53.
- 810 Barber, C. B., D. P. Dobkin, and H. Huhdanpaa (1996), The quickhull algorithm for con-
811 vex hulls, *ACM Transactions on Mathematical Software (TOMS)*, 22(4), 469–483.
- 812 Chirico, G. B., A. W. Western, R. B. Grayson, and G. Blöschl (2005), On the definition
813 of the flow width for calculating specific catchment area patterns from gridded elevation
814 data, *Hydrological Processes*, 19(13), 2539–2556.
- 815 Du, C., A. Ye, Y. Gan, J. You, Q. Duan, F. Ma, and J. Hou (2017), Drainage network ex-
816 traction from a high-resolution DEM using parallel programming in the .NET framework,
817 *Journal of Hydrology*, 555, 506–517.

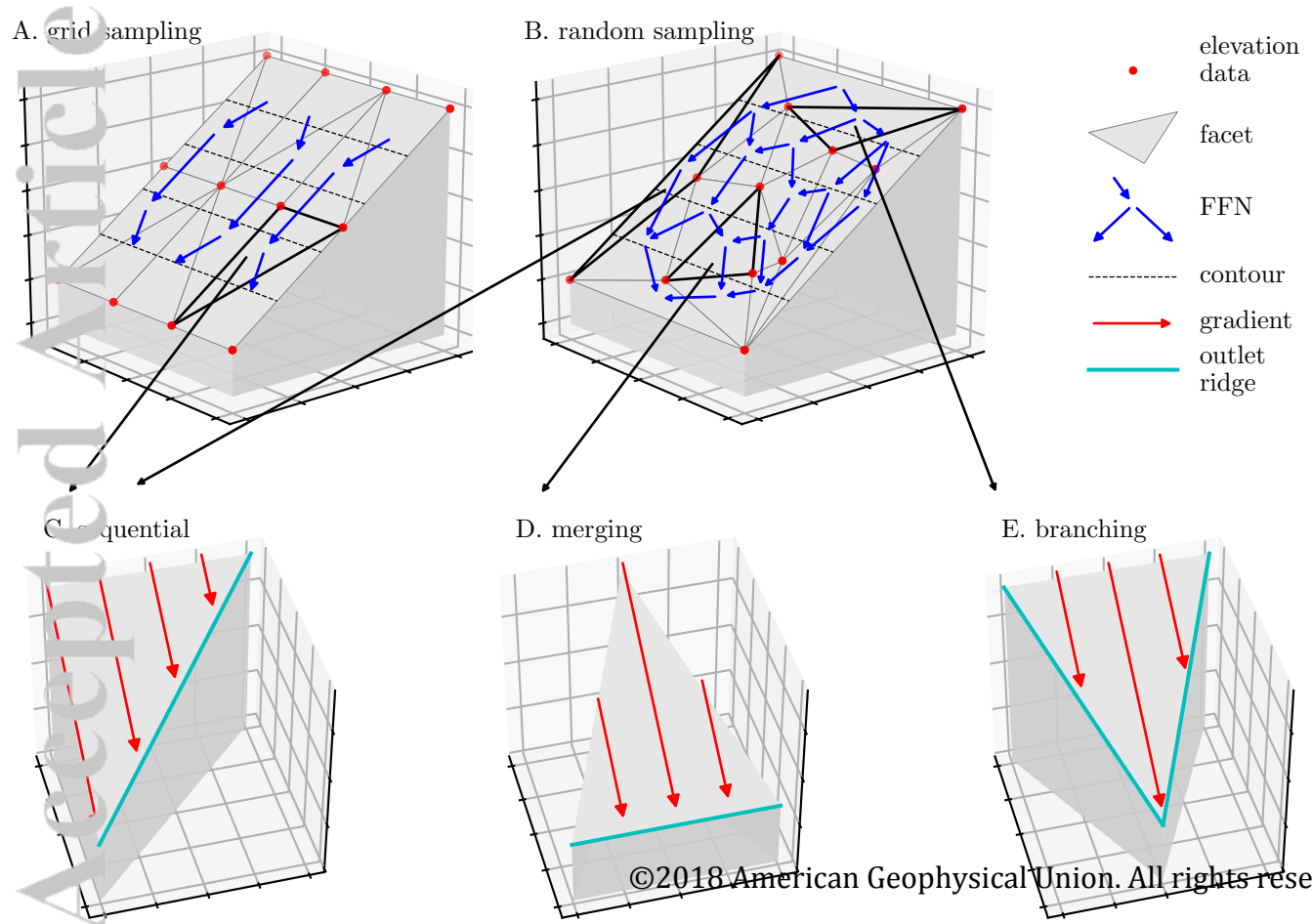
- 818 Erskine, R. H., T. R. Green, J. A. Ramirez, and L. H. MacDonald (2006), Comparison
19 of grid-based algorithms for computing upslope contributing area, *Water Resources Re-*
820 *search*, 42(9).
- 821 Fisher, G. B., B. Bookhagen, and C. B. Amos (2013), Channel planform geometry and
22 slopes from freely available high-spatial resolution imagery and DEM fusion: Implica-
823 tions for channel width scalings, erosion proxies, and fluvial signatures in tectonically
24 active landscapes, *Geomorphology*, 194, 46–56.
- 25 Florinsky, I. V. (1998), Accuracy of local topographic variables derived from digital eleva-
826 tion models, *International Journal of Geographical Information Science*, 12(1), 47–62.
- 27 Freeman, T. G. (1991), Calculating catchment area with divergent flow based on a regular
828 grid, *Computers & Geosciences*, 17(3), 413–422.
- 29 Gallant, J. C., and M. F. Hutchinson (2011), A differential equation for specific catchment
830 area, *Water Resources Research*, 47(5).
- 31 Hilley, G. E., and J. R. Arrowsmith (2008), Geomorphic response to uplift along the
832 dragon's back pressure ridge, Carrizo plain, California, *Geology*, 36(5), 367.
- 33 Hurst, M. D., S. M. Mudd, R. Walcott, M. Attal, and K. Yoo (2012), Using hilltop curva-
834 ture to derive the spatial distribution of erosion rates, *Journal of Geophysical Research: Earth
835 Surface*, 117(F2), F02017.
- 36 Ivanov, V. Y., E. R. Vivoni, R. L. Bras, and D. Entekhabi (2004), Catchment hydrologic
37 response with a fully distributed triangulated irregular network model, *Water Resources
838 Research*, 40(11), w11102.
- 39 Jenson, S. K., and J. O. Domingue (1988), Extracting topographic structure from digital
40 elevation data for geographic information system analysis, *Photogrammetric Engineering
and Remote Sensing*, 54(11), 1593–1600.
- 42 Jones, N. L., S. G. Wright, and D. R. Maidment (1990), Watershed delineation with
43 triangle-based terrain models, *Journal of Hydraulic Engineering*, 116(10), 1232–1251.
- 44 Larsen, L. G., M. B. Eppinga, P. Passalacqua, W. M. Getz, K. A. Rose, and M. Liang
45 (2016), Appropriate complexity landscape modeling, *Earth-Science Reviews*, 160(C),
846 111–130.
- 47 Ludwig, J. A., B. P. Wilcox, D. D. Breshears, D. J. Tongway, and A. C. Imeson (2005),
848 Vegetation patches and runoff–erosion as interacting ecohydrological processes in semi-
arid landscapes, *Ecology*, 86(2), 288–297.
- 49 Meigs, A. (2013), Active tectonics and the lidar revolution, *Lithosphere*, 5(2), 226.

- Montgomery, D. R., and E. Foufoula-Georgiou (1993), Channel network source representation using digital elevation models, *Water Resources Research*, 29(12), 3925–3934.
- Neely, A. B., B. Bookhagen, and D. W. Burbank (2017), An automated knickzone selection algorithm (KZ-Picker) to analyze transient landscapes: Calibration and validation, *Journal of Geophysical Research: Earth Surface*, 122(6), 1236–1261.
- NSF OpenTopography Facility (2012), 2010 channel islands lidar collection, doi:10.5069/g95d8ps7.
- O'Callaghan, J. F., and D. M. Mark (1984), The extraction of drainage networks from digital elevation data, *Computer Vision, Graphics, and Image Processing*, 28(3), 323–344.
- Oksanen, J., and T. Sarjakoski (2006), Uncovering the statistical and spatial characteristics of fine toposcale dem error, *International Journal of Geographical Information Science*, 20(4), 345–369.
- Passalacqua, P., P. Tarolli, and E. Foufoula-Georgiou (2010), Testing space-scale methodologies for automatic geomorphic feature extraction from lidar in a complex mountainous landscape, *Water Resources Research*, 46(11), w11535.
- Passalacqua, P., P. Belmont, D. M. Staley, J. D. Simley, J. R. Arrowsmith, C. A. Bode, C. Crosby, S. B. DeLong, N. F. Glenn, S. A. Kelly, D. Lague, H. Sangireddy, K. Schaftrath, D. G. Tarboton, T. Wasklewicz, and J. M. Wheaton (2015), Analyzing high resolution topography for advancing the understanding of mass and energy transfer through landscapes: A review, *Earth-Science Reviews*, 148(C), 174–193.
- Pelletier, J. (2012), Mfdrouting, doi:10.1594/ieda/100145.
- Pelletier, J. D. (2008), *Quantitative modeling of earth surface processes*, vol. 304, Cambridge University Press Cambridge.
- Pelletier, J. D. (2010), Minimizing the grid-resolution dependence of flow-routing algorithms for geomorphic applications, *Geomorphology*, 122(1-2), 91–98.
- Perroy, R. L., B. Bookhagen, G. P. Asner, and O. A. Chadwick (2010), Comparison of gully erosion estimates using airborne and ground-based LiDAR on Santa Cruz Island, California, *Geomorphology*, 118(3), 288–300.
- Perroy, R. L., B. Bookhagen, O. A. Chadwick, and J. T. Howarth (2012), Holocene and Anthropocene landscape change: Arroyo formation on Santa Cruz Island, California, *Annals of the Association of American Geographers*, 102(6), 1229–1250.
- Planchon, O., and F. Darboux (2002), A fast, simple and versatile algorithm to fill the depressions of digital elevation models, *CATENA*, 46(2), 159–176.

- 884 Qin, C., A.-X. Zhu, T. Pei, B. Li, C. Zhou, and L. Yang (2007), An adaptive approach to
885 selecting a flow-partition exponent for a multiple-flow-direction algorithm, *International*
886 *Journal of Geographical Information Science*, 21(4), 443–458.
- 887 Rengers, F. K., L. A. McGuire, J. A. Coe, J. W. Kean, R. L. Baum, D. M. Staley, and
888 J. W. Godt (2016), The influence of vegetation on debris-flow initiation during extreme
889 rainfall in the northern Colorado front range, *Geology*, 44(10), 823–826.
- 890 Rieger, W. (1993), Automated river line and catchment area extraction from DEM data,
891 *Int. Arch. Photogramm. Remote Sens.*, 29, 642–642.
- 892 Roering, J. J., B. H. Mackey, J. A. Marshall, K. E. Sweeney, N. I. Deligne, A. M. Booth,
893 A. L. Handwerger, and C. Cerovski-Darriaud (2013), ‘You are HERE’: Connecting the
894 dots with airborne lidar for geomorphic fieldwork, *Geomorphology*, 200, 172–183.
- 895 Schoorl, J., M. Sonneveld, and A. Veldkamp (2000), Three-dimensional landscape process
896 modelling: the effect of dem resolution, *Earth Surface Processes and Landforms: The*
897 *Journal of the British Geomorphological Research Group*, 25(9), 1025–1034.
- 898 Shelef, E., and G. E. Hilley (2013), Impact of flow routing on catchment area calculations,
899 slope estimates, and numerical simulations of landscape development, *Journal of Geo-*
900 *physical Research: Earth Surface*, 118(4), 2105–2123.
- 901 Soille, P., J. Vogt, and R. Colombo (2003), Carving and adaptive drainage enforcement of
902 grid digital elevation models, *Water Resources Research*, 39(12), 1366.
- 903 Tarboton, D. G. (1997), A new method for the determination of flow directions and ups-
904 lope areas in grid digital elevation models, *Water Resources Research*, 33(2), 309–319.
- 905 Tarolli, P., J. R. Arrowsmith, and E. R. Vivoni (2009), Understanding earth surface pro-
906 cesses from remotely sensed digital terrain models, *Geomorphology*, 113(1), 1–3.
- 907 Tucker, G. E., and R. L. Bras (1998), Hillslope processes, drainage density, and landscape
908 morphology, *Water Resources Research*, 34(10), 2751–2764.
- 909 Wang, Y., H. Peng, P. Cui, W. Zhang, F. Qiao, and C. Chen (2009), A new treatment of
910 depression for drainage network extraction based on dem, *Journal of Mountain Science*,
911 6(4), 311–319.
- 912 Wechsler, S. (2007), Uncertainties associated with digital elevation models for hydrologic
913 applications: a review, *Hydrology and Earth System Sciences*, 11(4), 1481–1500.
- 914 Wechsler, S. P., and C. N. Kroll (2006), Quantifying dem uncertainty and its effect on
915 topographic parameters, *Photogrammetric Engineering & Remote Sensing*, 72(9), 1081–
916 1090.

- 917 Zhang, F., Q. Zhou, Q. Li, G. Wu, and J. Liu (2017), An enhanced approach for surface
918 flow routing over drainage-constrained triangulated irregular networks, *Transactions in*
919 *GIS*.
- 920 Zhou, Q., and X. Liu (2002), Error assessment of grid-based flow routing algorithms used
921 in hydrological models, *International journal of geographical information science*, 16(8),
922 819–842.
- 923 Zhou, Q., P. Pilesjö, and Y. Chen (2011), Estimating surface flow paths on a digital eleva-
924 tion model using a triangular facet network, *Water Resources Research*, 47(7).

Accepted Article



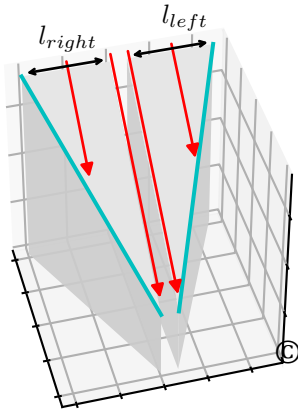
Accepted Article

E1. branching

$$l_{orig} = l_{left} + l_{right}$$

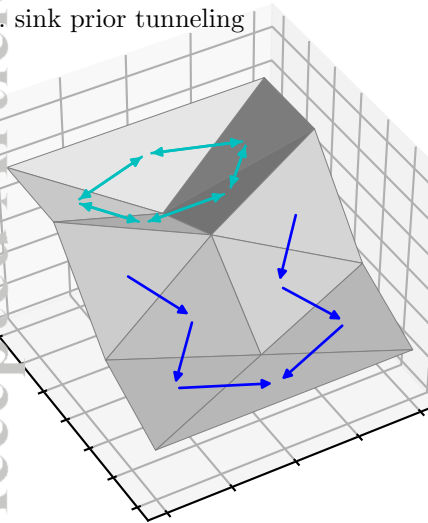
\Leftrightarrow

E2. cut into two sequential

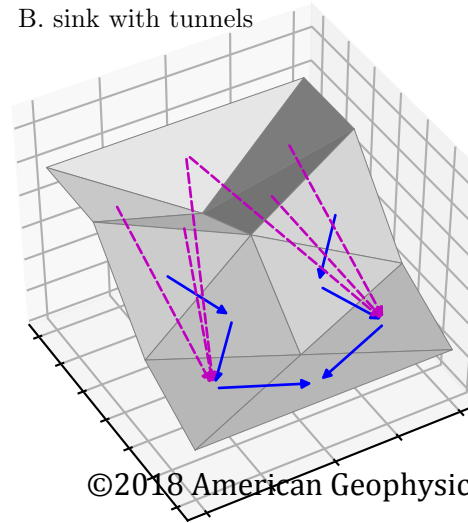


Accepted Article

A. sink prior tunneling

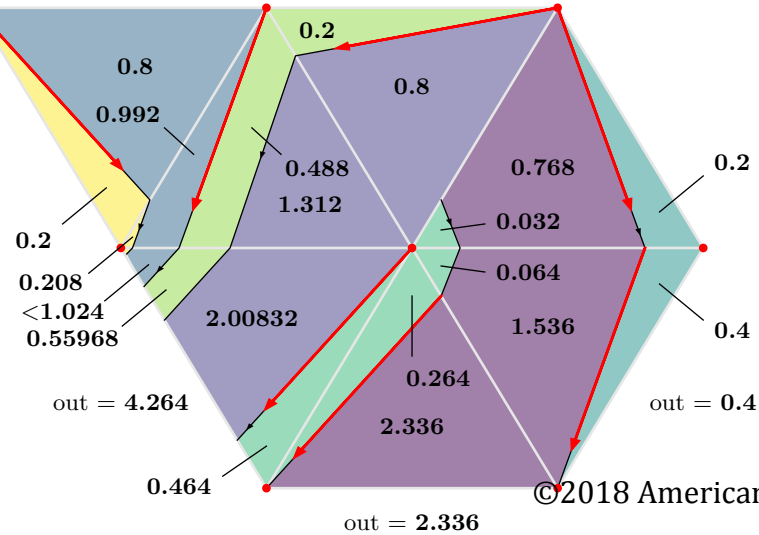


B. sink with tunnels

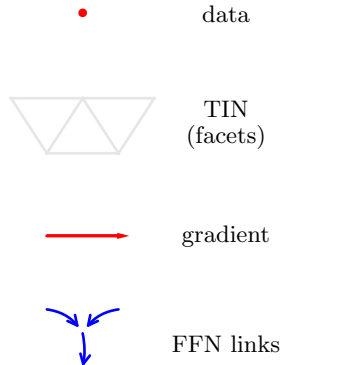
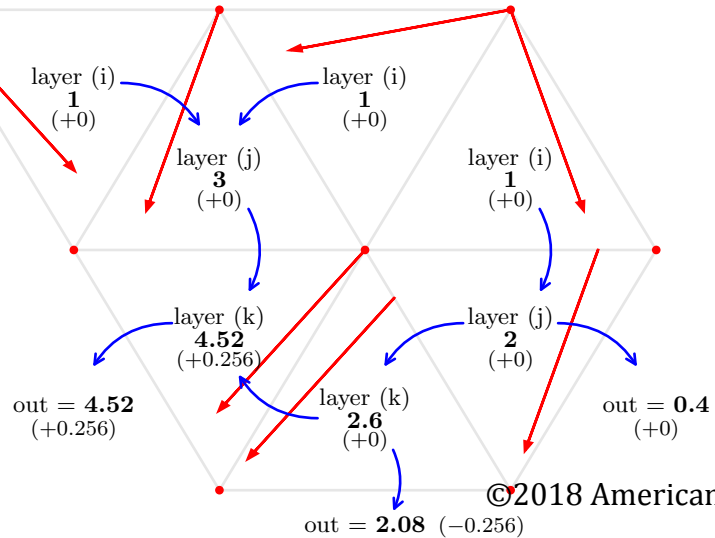


- ↔ sink link
- tunnel
- FFN

Accepted Article

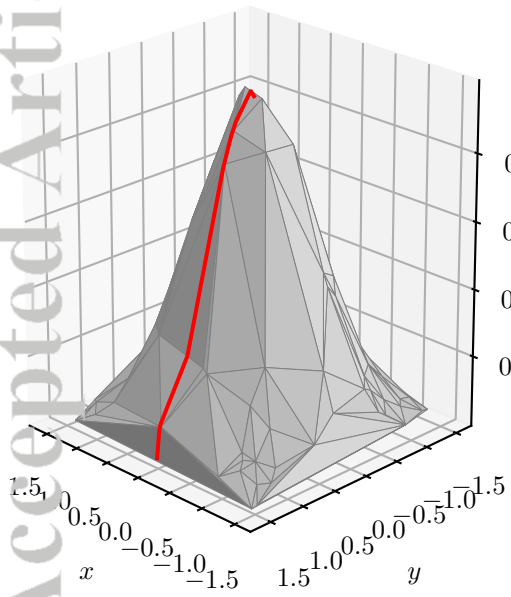


Accepted Article

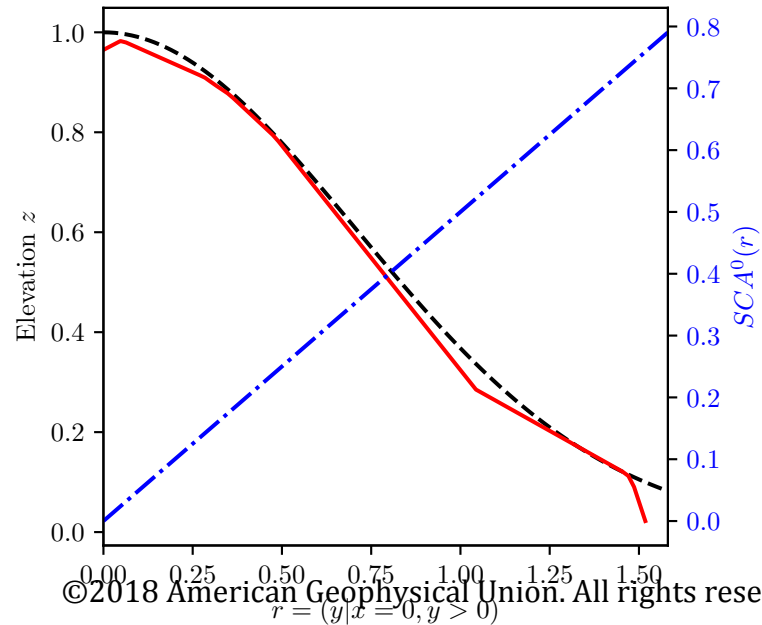


4.52 FFN TDA value
+0.256

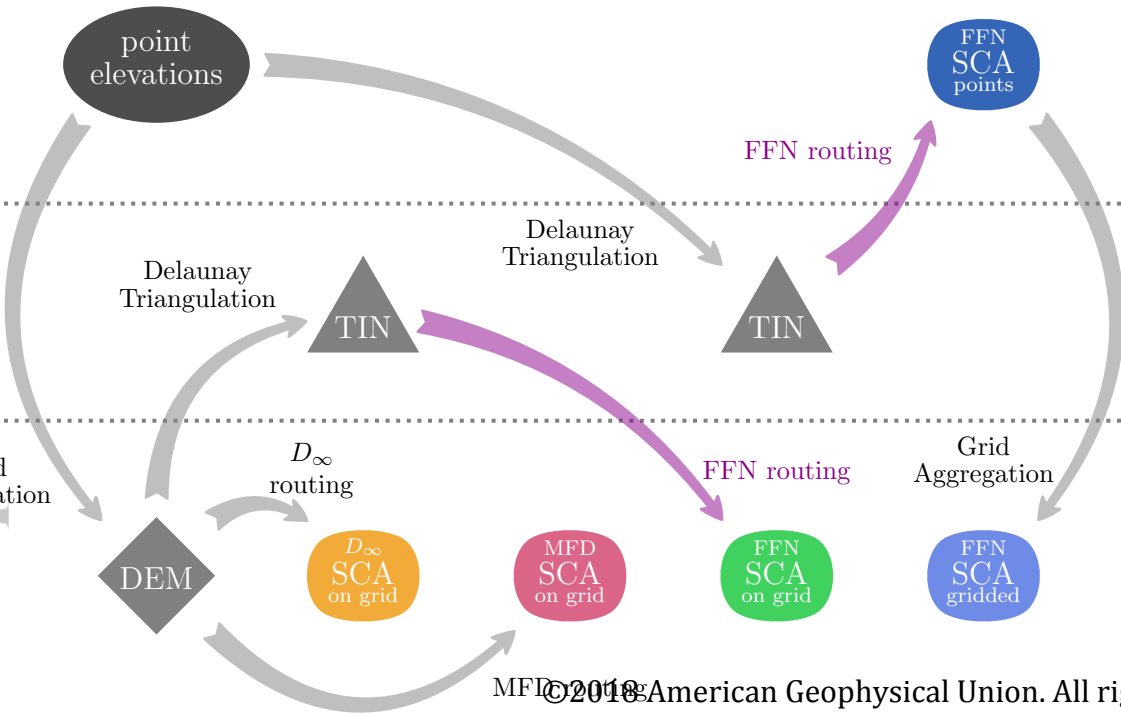
Accepted Article



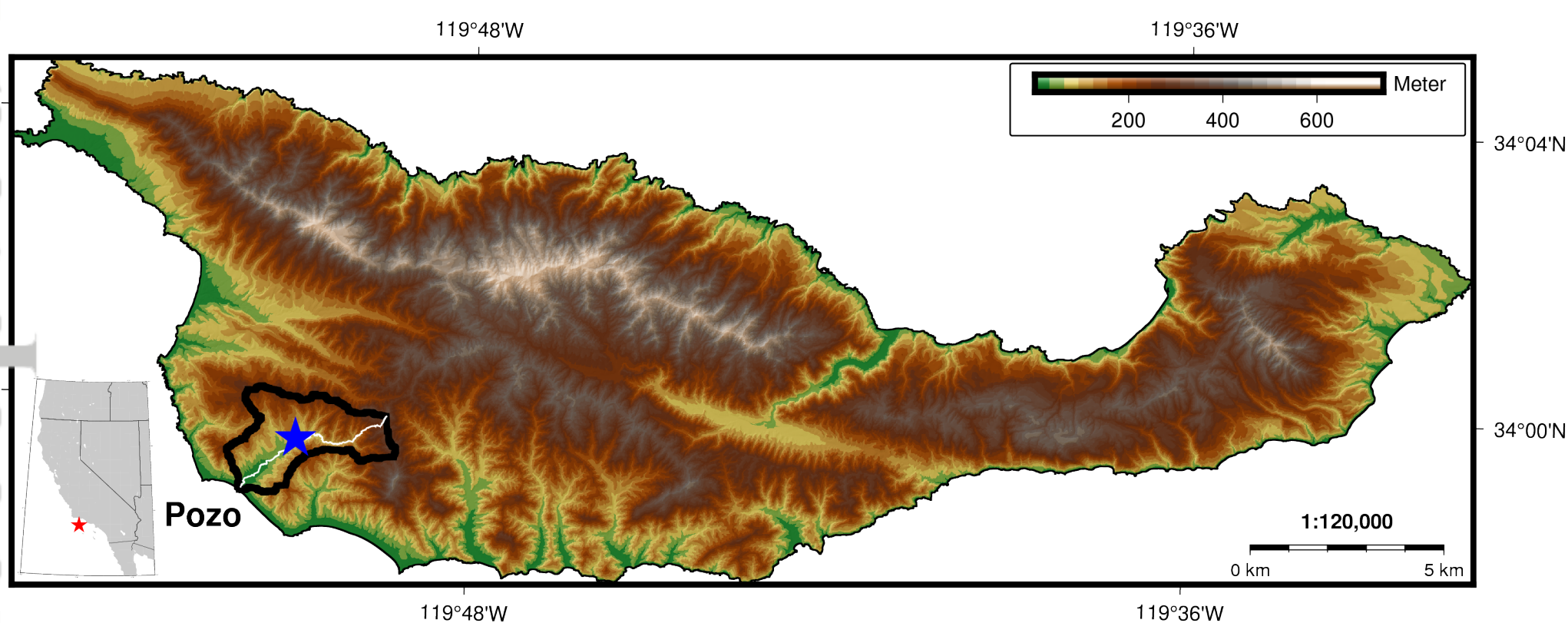
— $SCA^0(r) = r/2$ - - - Gaussian profile
 $z(r) = e^{-r^2}$ — sampled profile
 $\rho = 10$



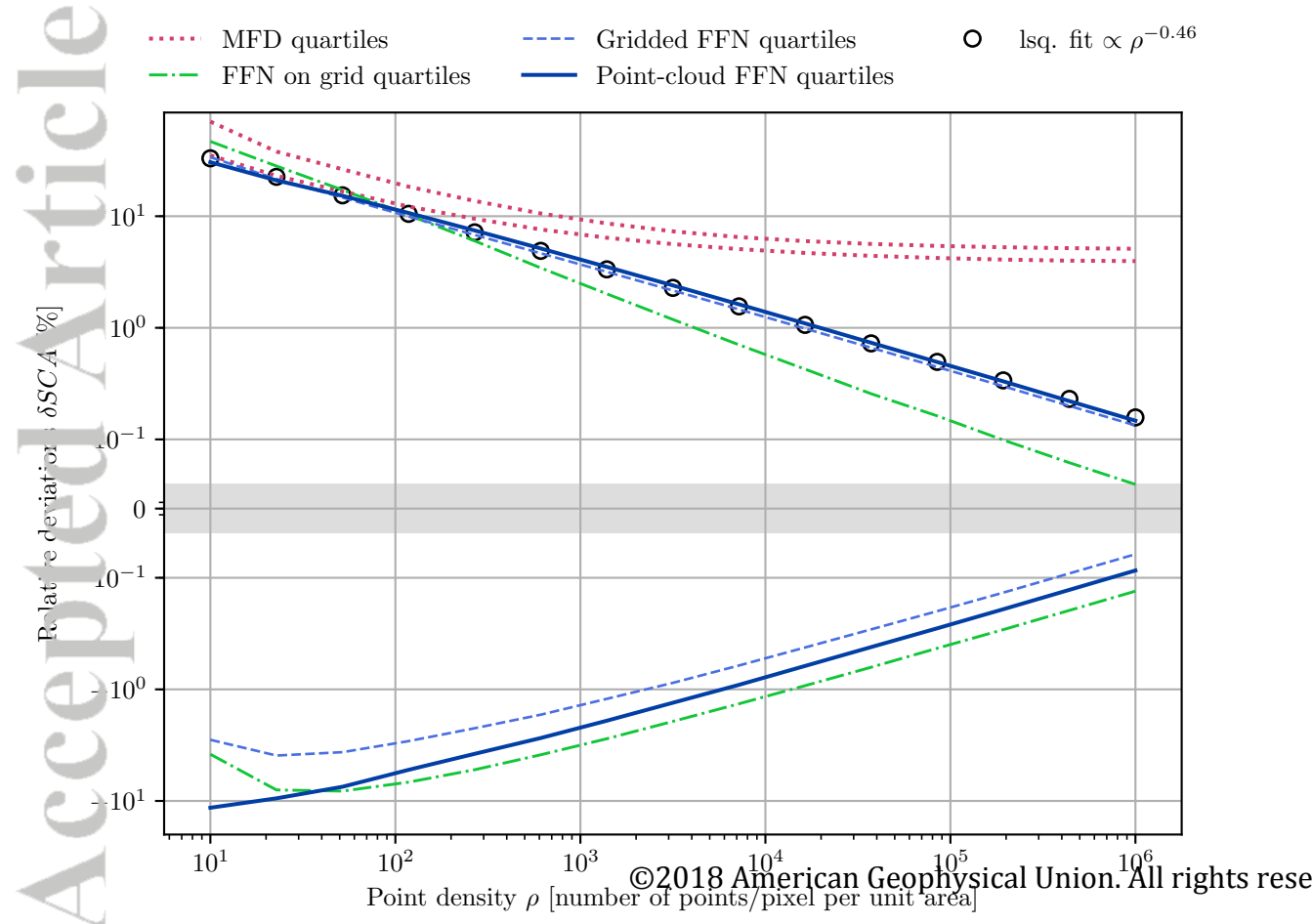
Accepted Article



Accepted Article

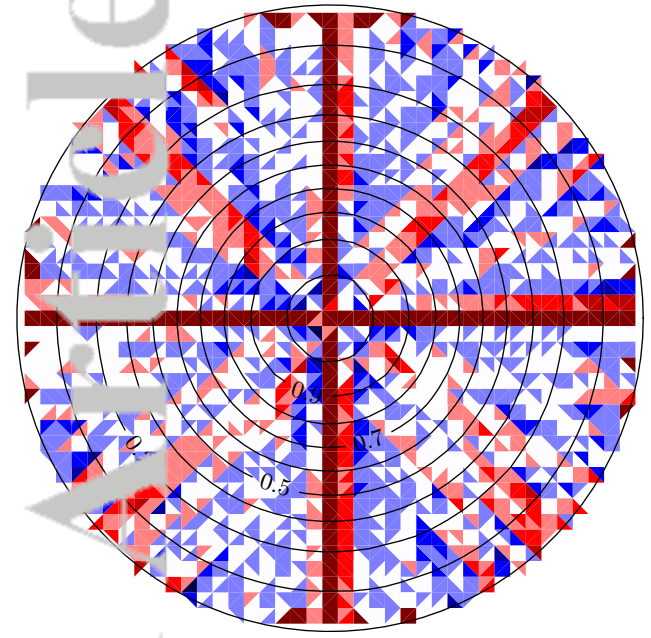


Accepted Article

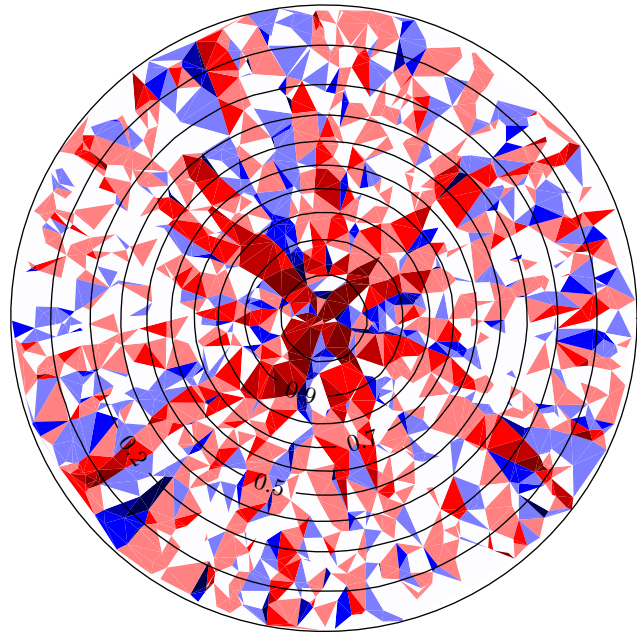


Accepted Article

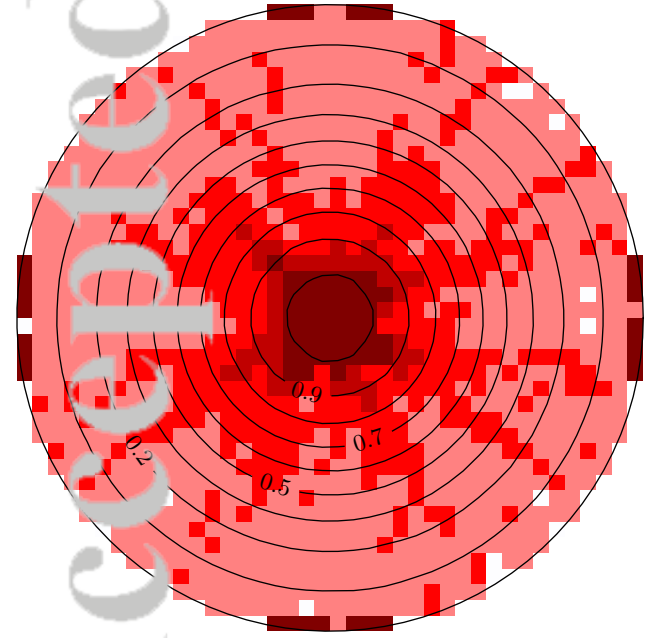
A. FFN of gridded DEM from point cloud



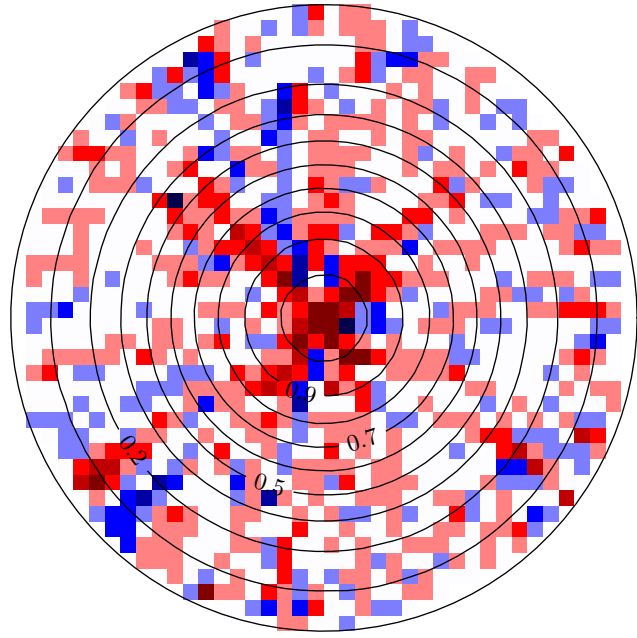
B. FFN of point cloud data directly



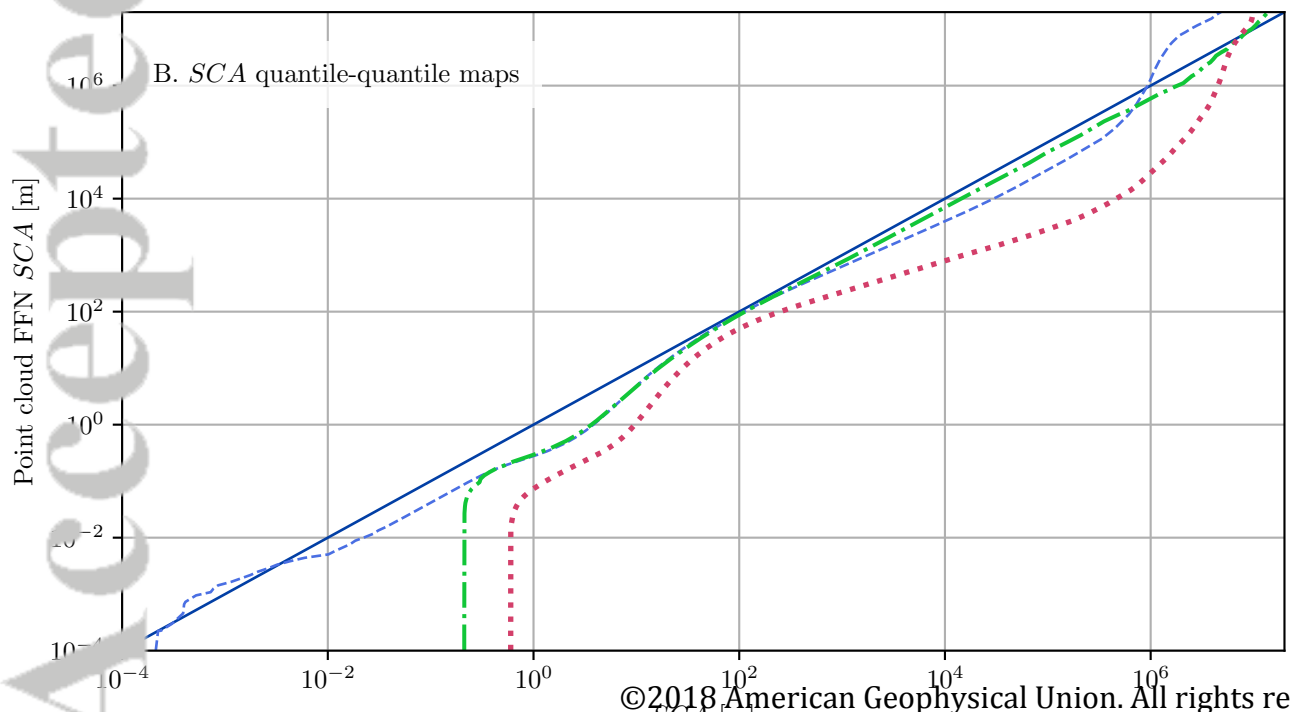
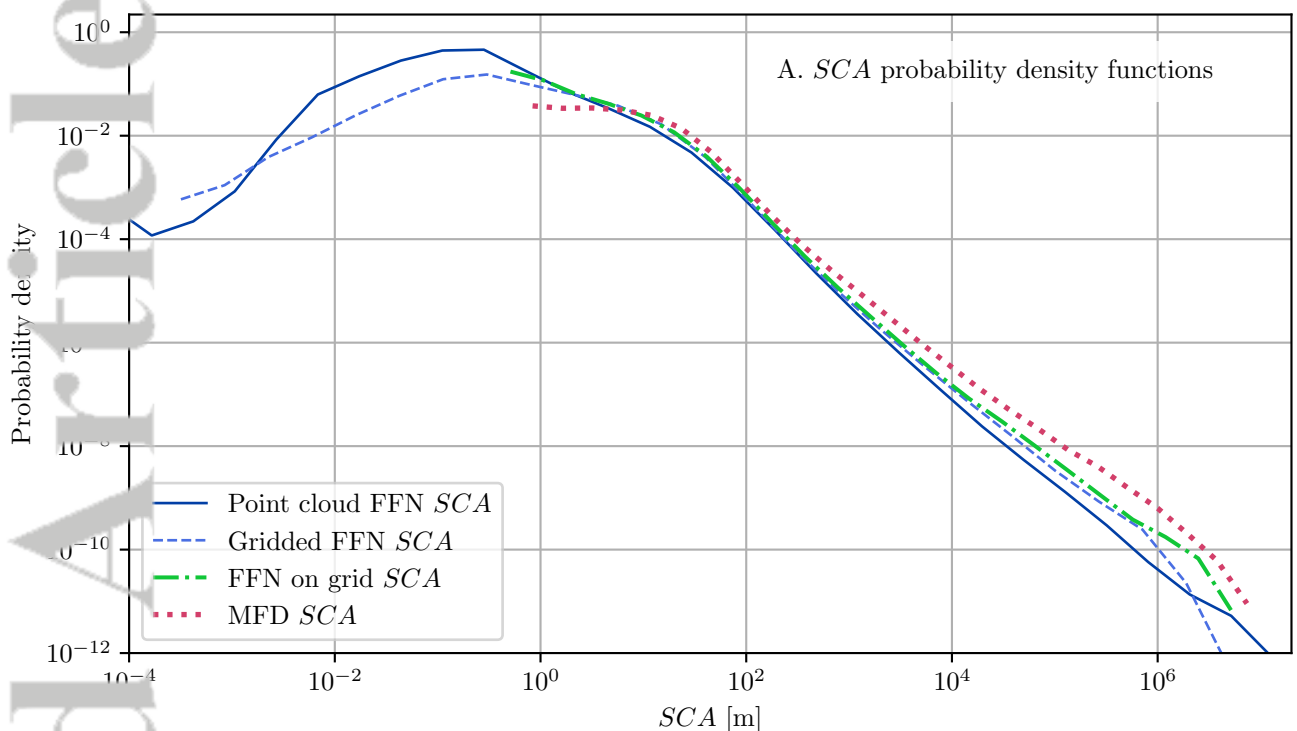
C. gridded DEM from point cloud



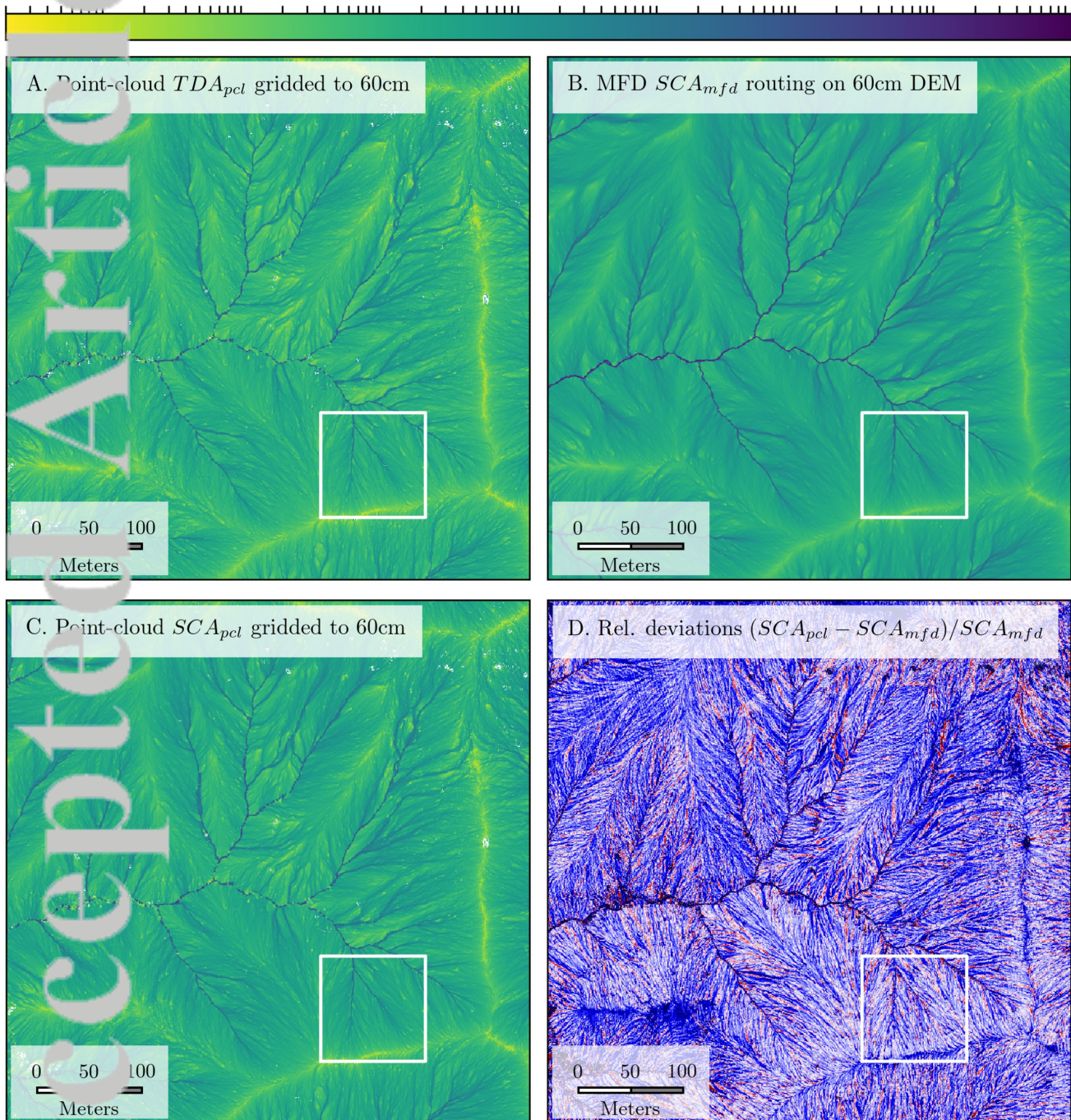
D. gridded version of B



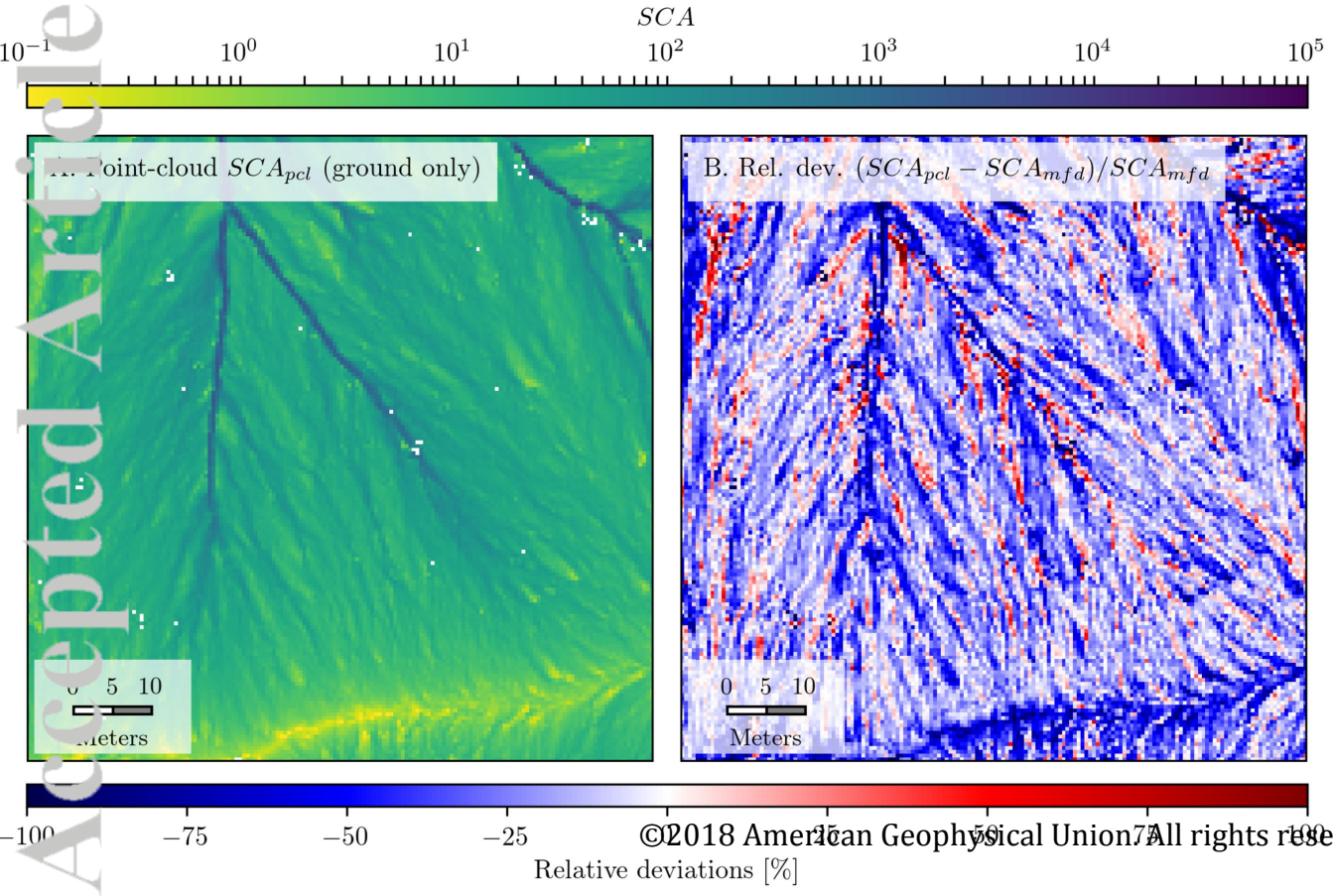
Accepted Article



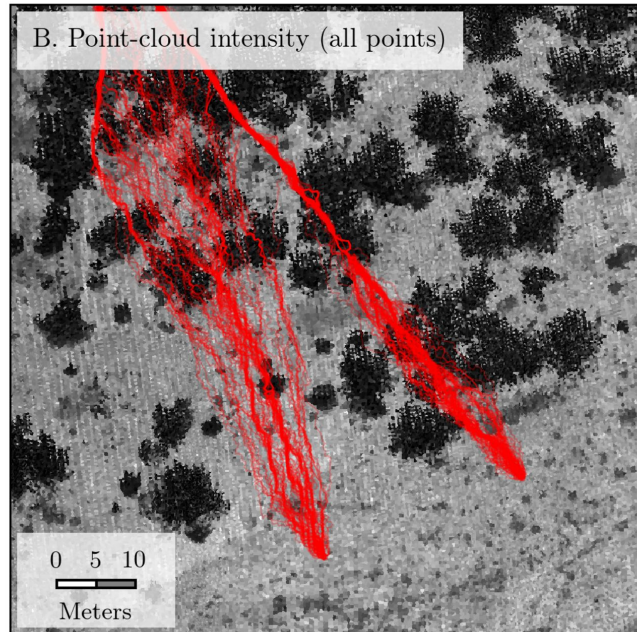
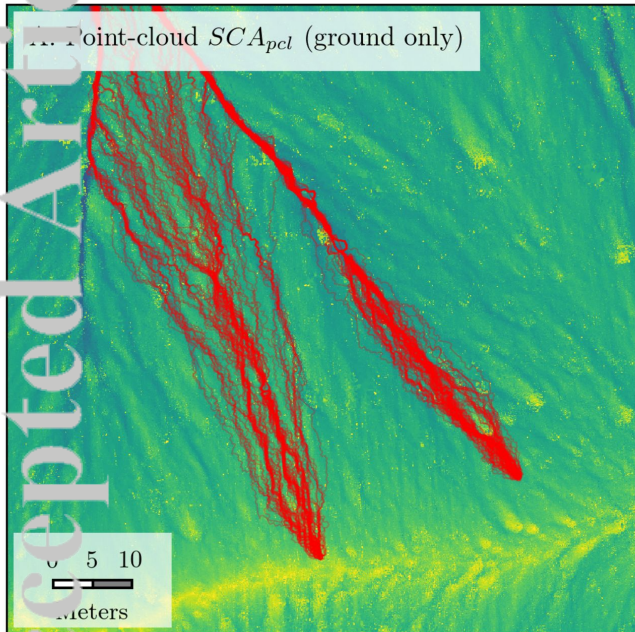
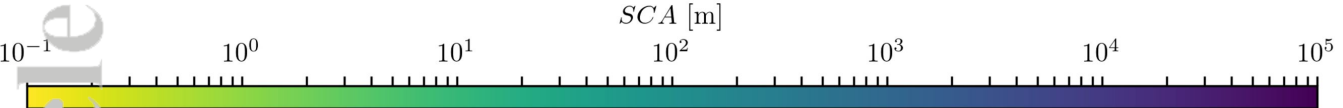
Accepted Article



Accepted Article



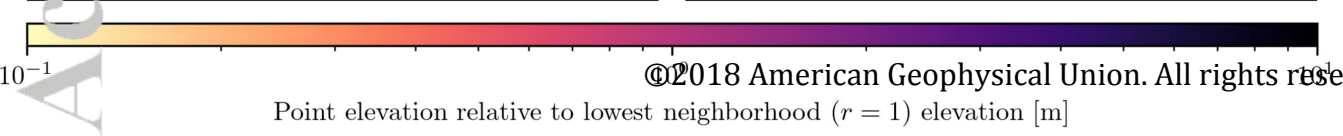
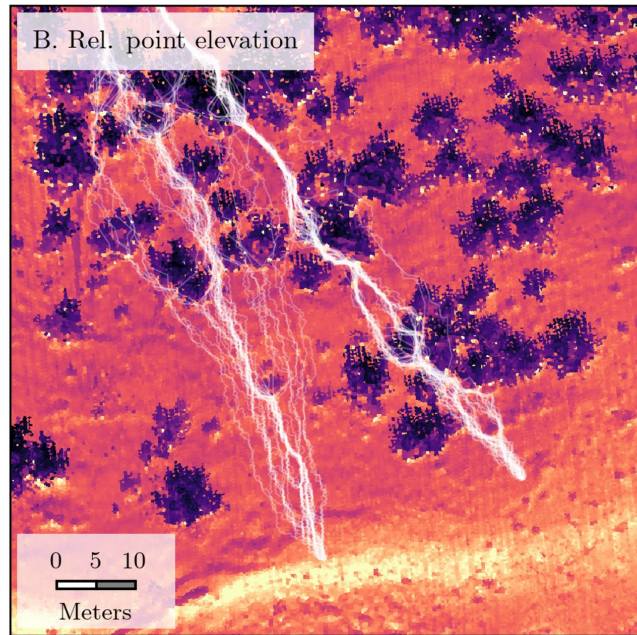
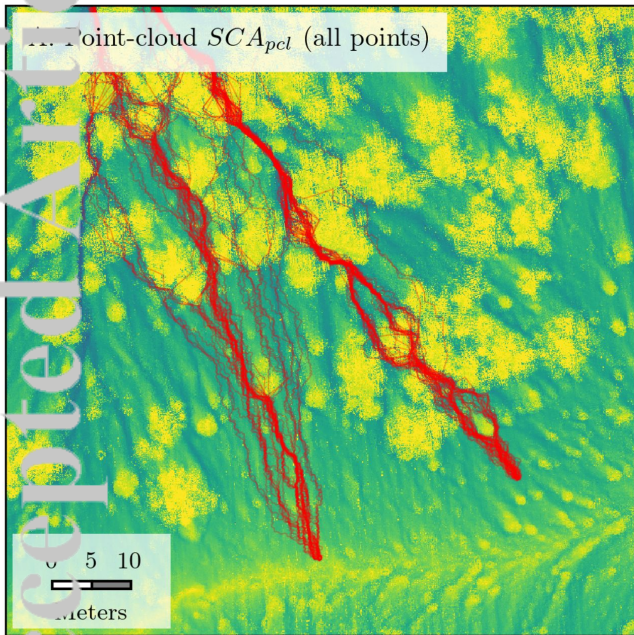
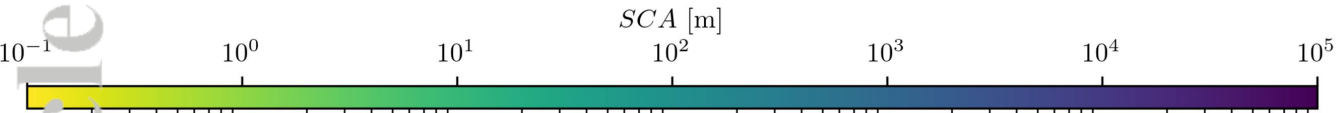
Accepted Article



Point-cloud intensity

©2018 American Geophysical Union. All rights reserved.

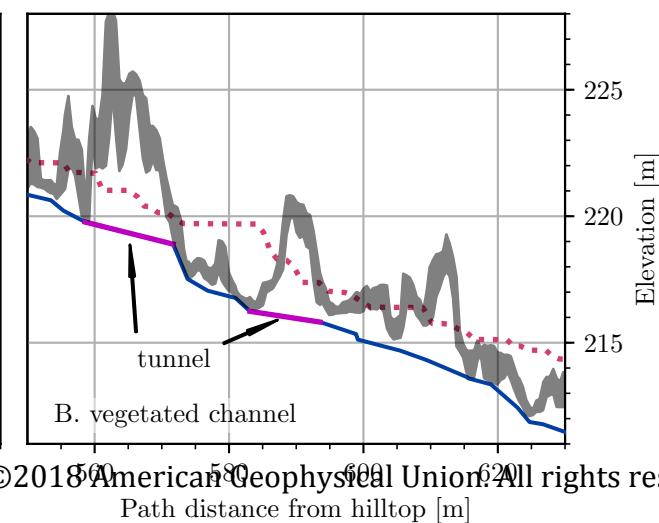
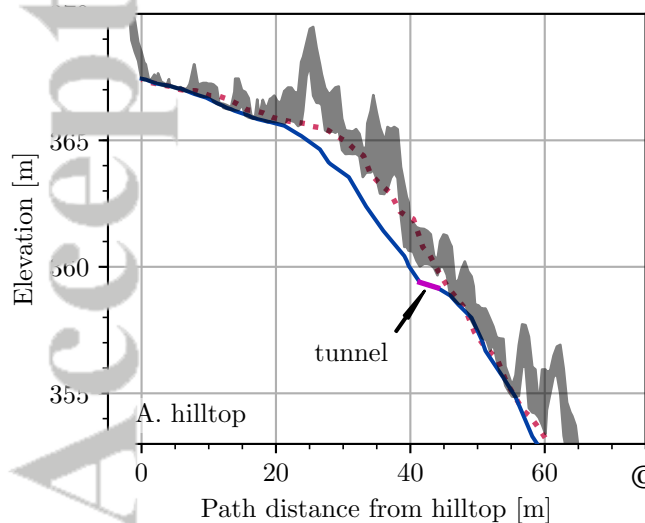
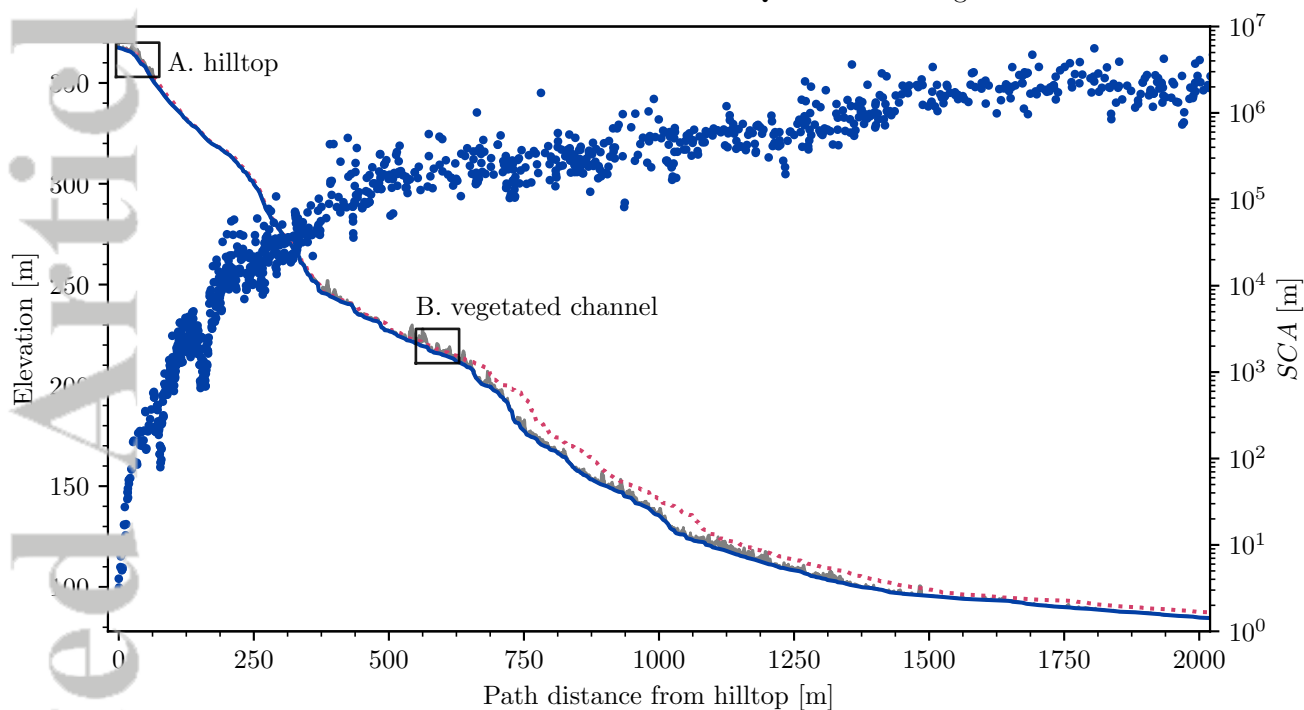
Accepted Article

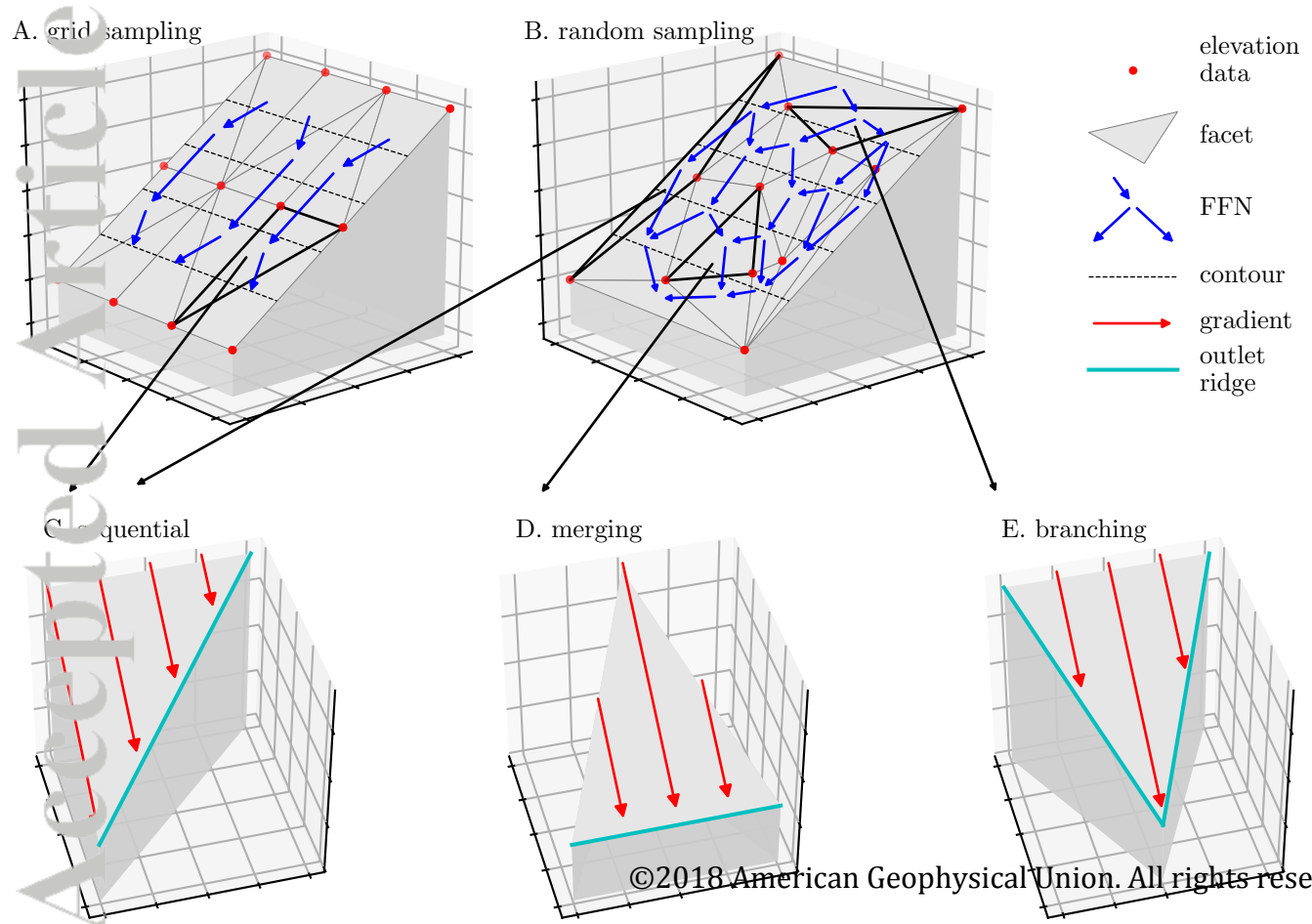


Accepted Article

MFD elevation
Point cloud FFN elevation

Point cloud FFN *SCA*
IQR of surrounding elevations



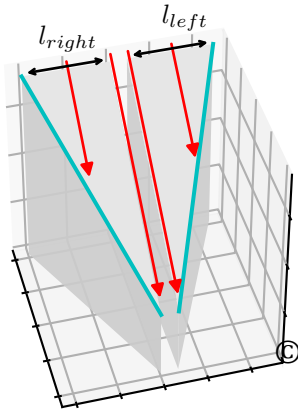


E1. branching

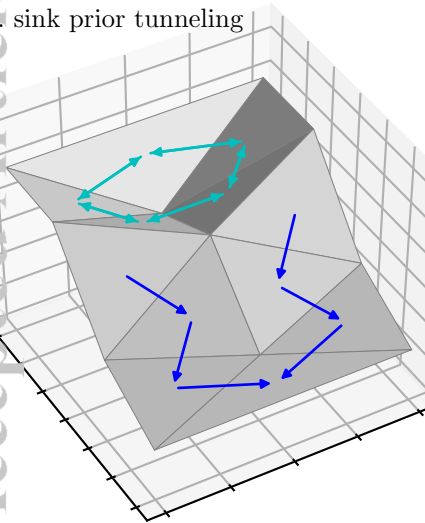
$$l_{orig} = l_{left} + l_{right}$$

\Leftrightarrow

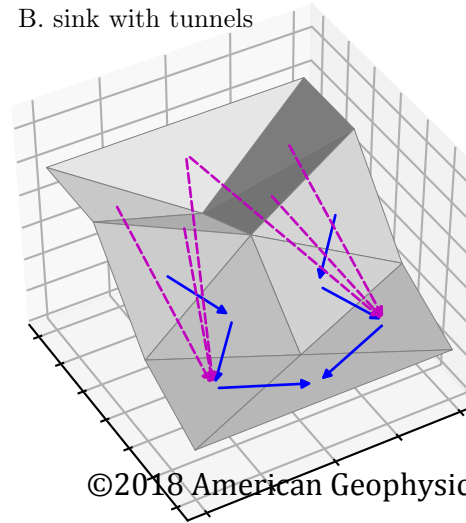
E2. cut into two sequential



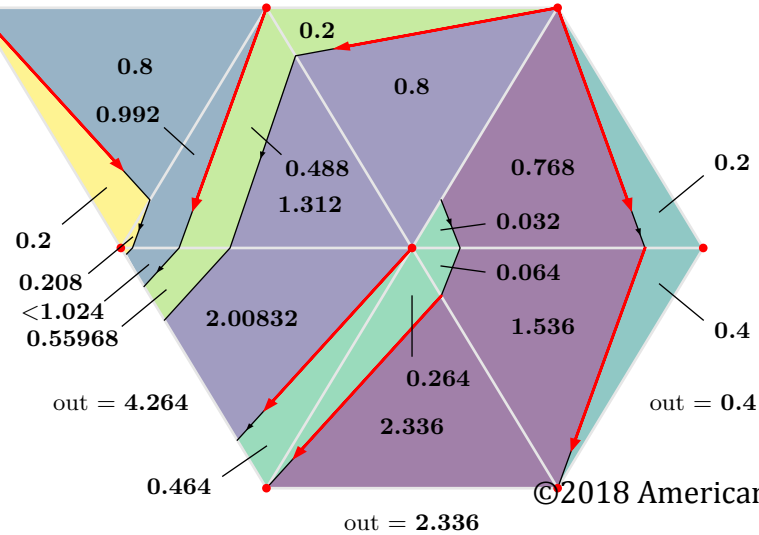
A. sink prior tunneling



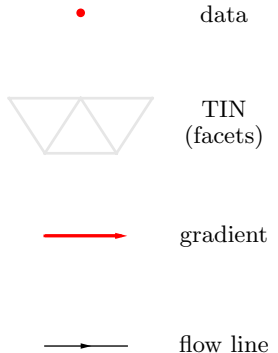
B. sink with tunnels

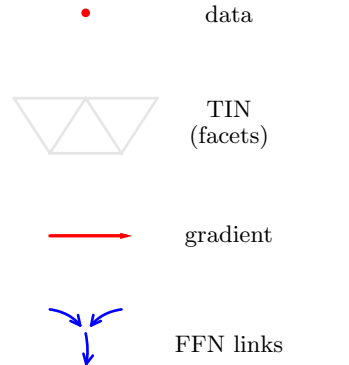
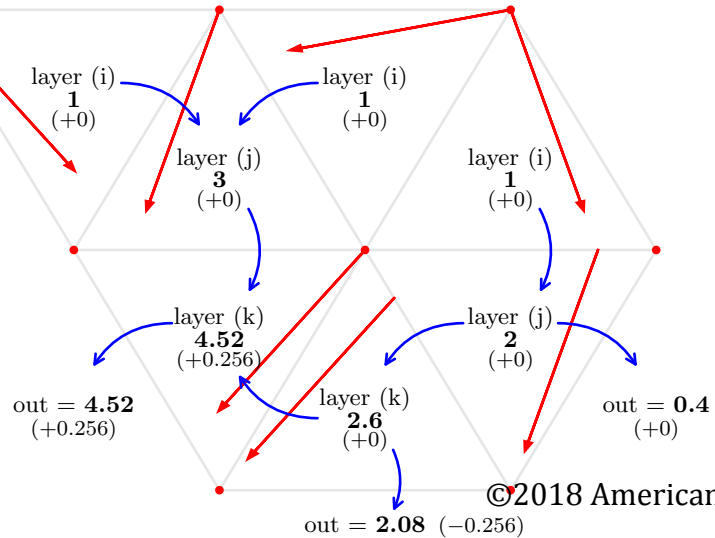


- ↔ sink link
- tunnel
- FFN

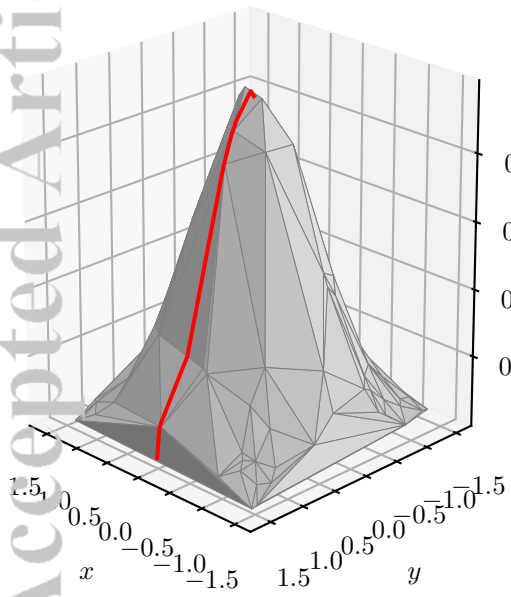


©2018 American Geophysical Union. All rights reserved.

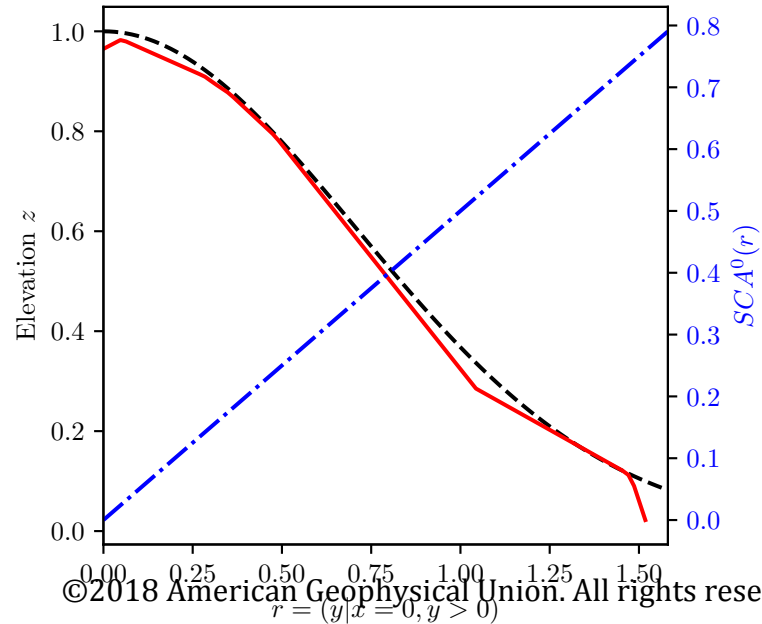


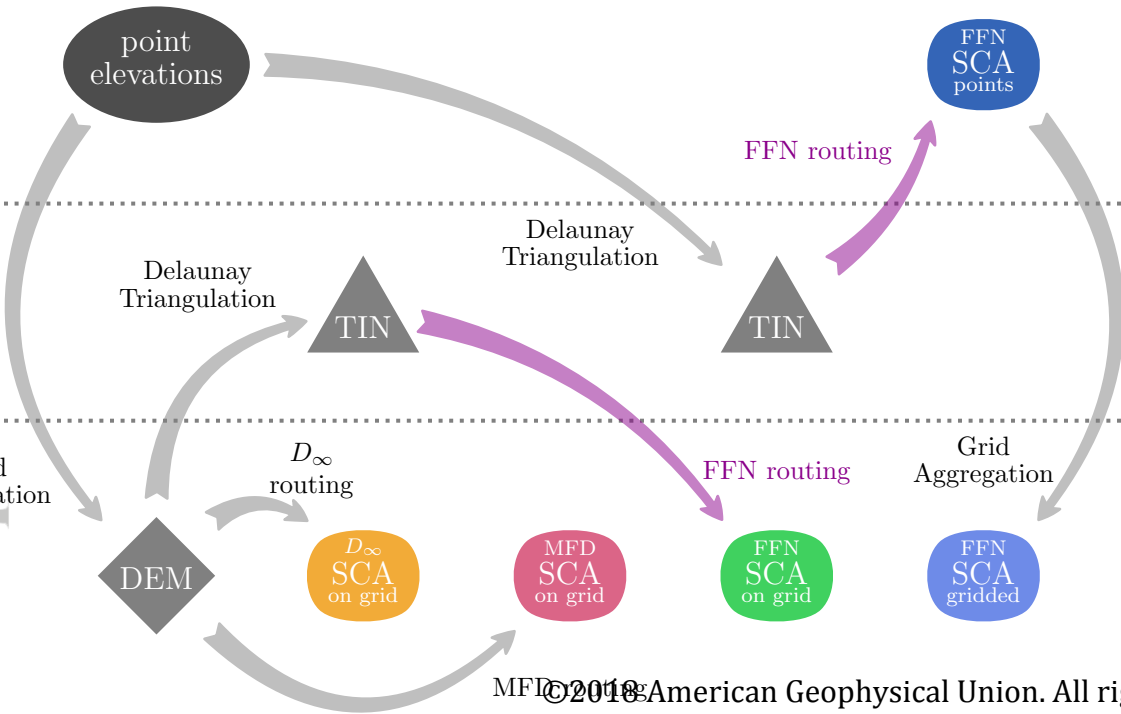


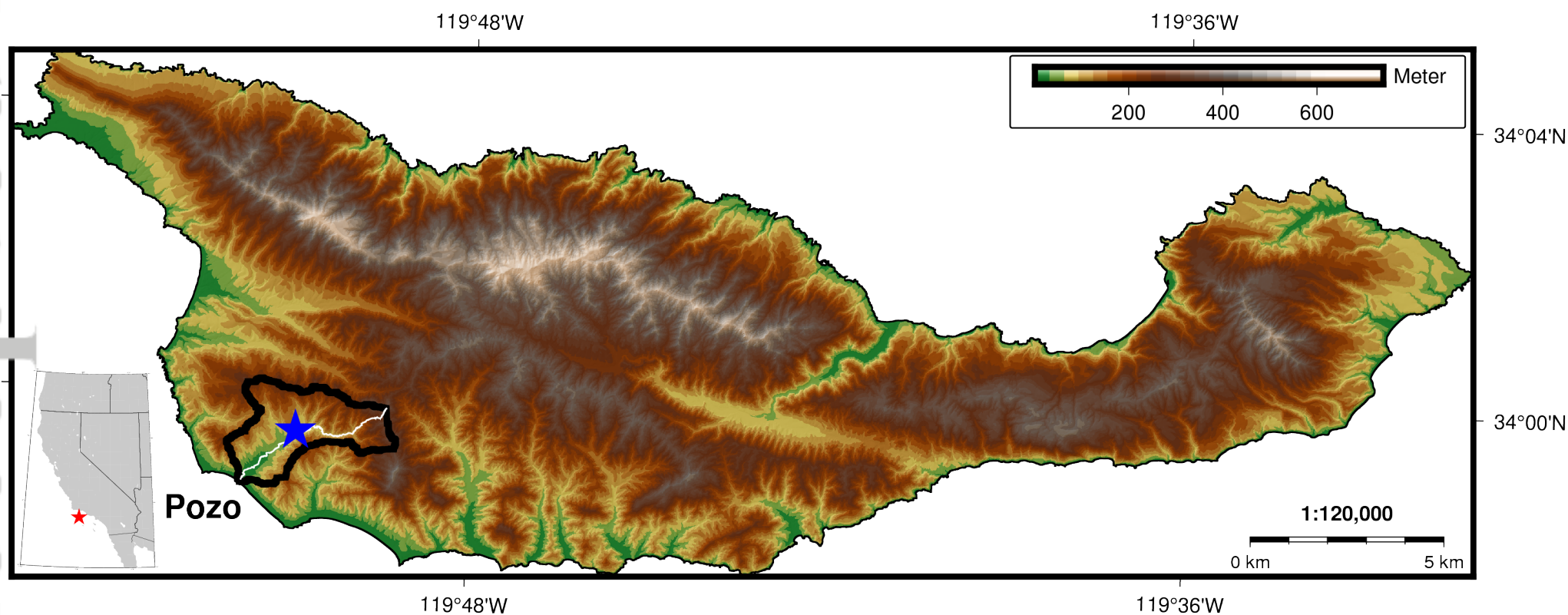
4.52 FFN TDA value
+0.256

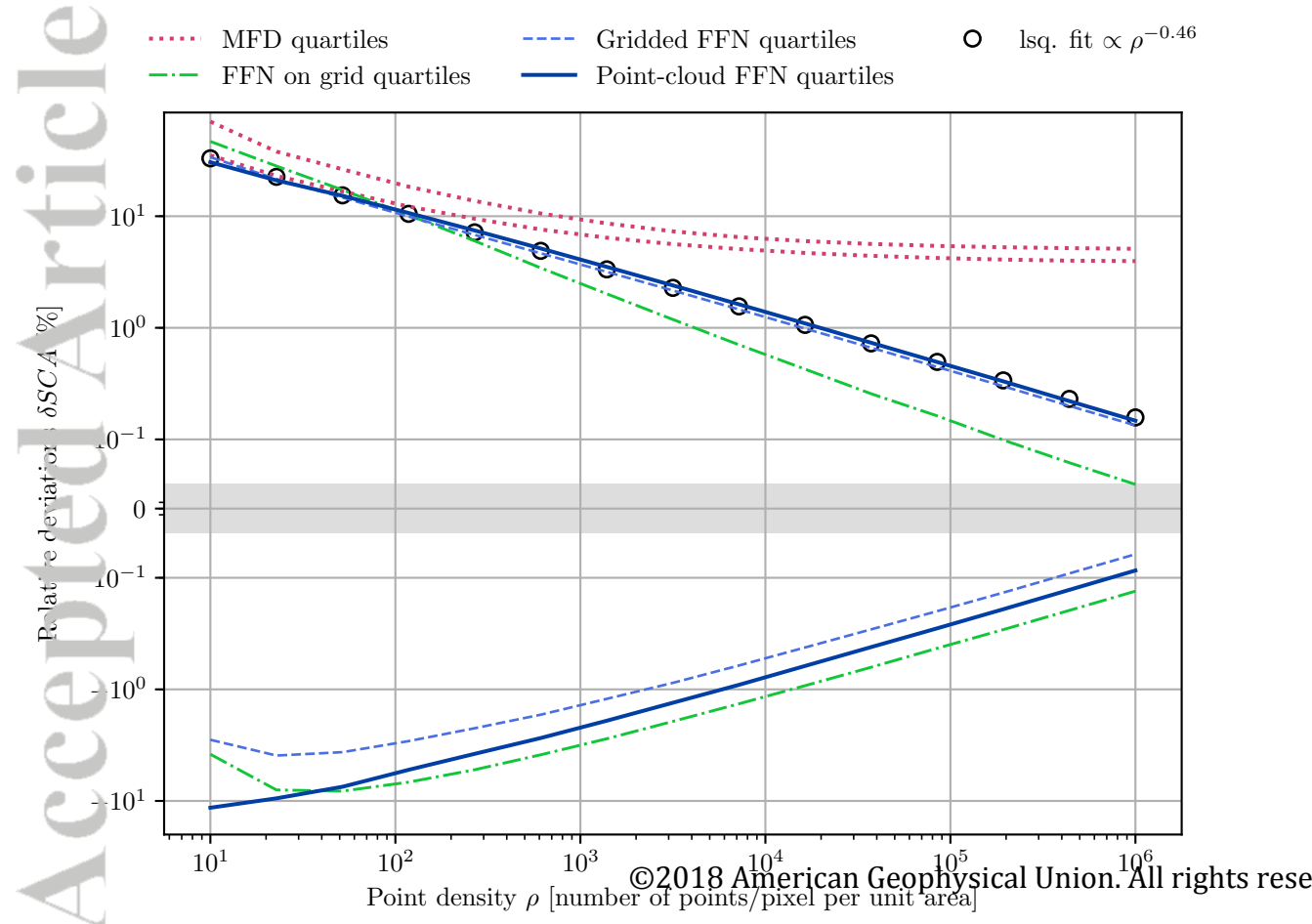


— $SCA^0(r) = r/2$ - - - Gaussian profile
 $z(r) = e^{-r^2}$ — sampled profile
 $\rho = 10$

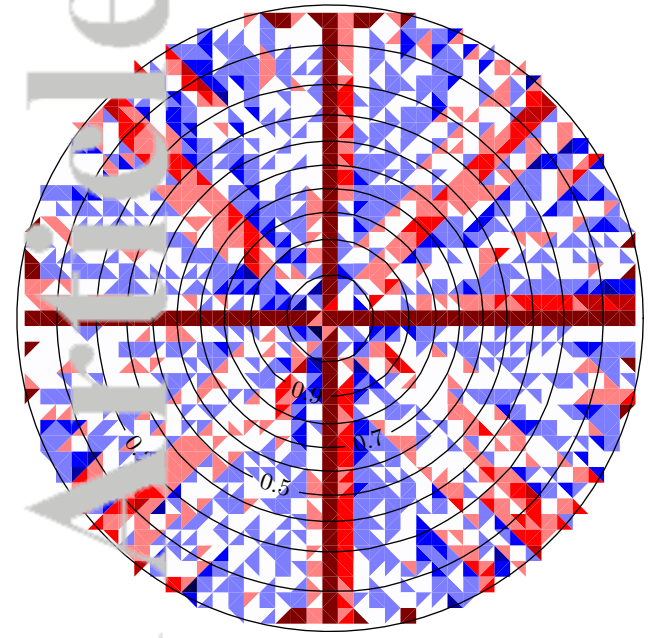




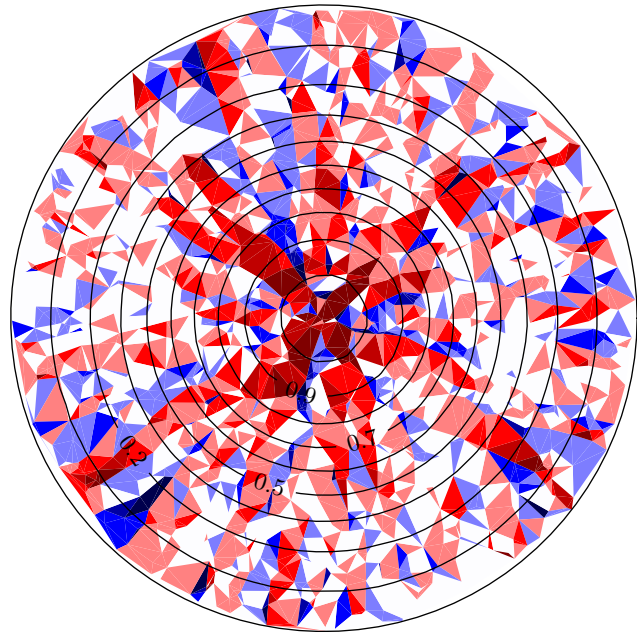




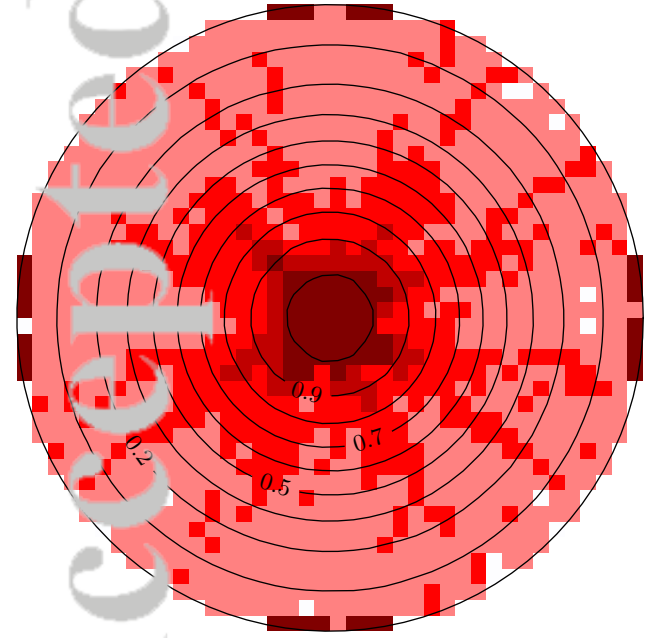
A. FFN of gridded DEM from point cloud



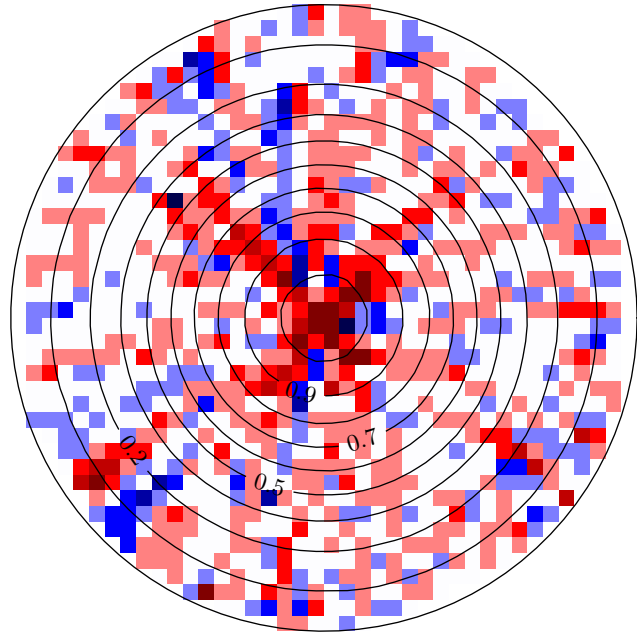
B. FFN of point cloud data directly

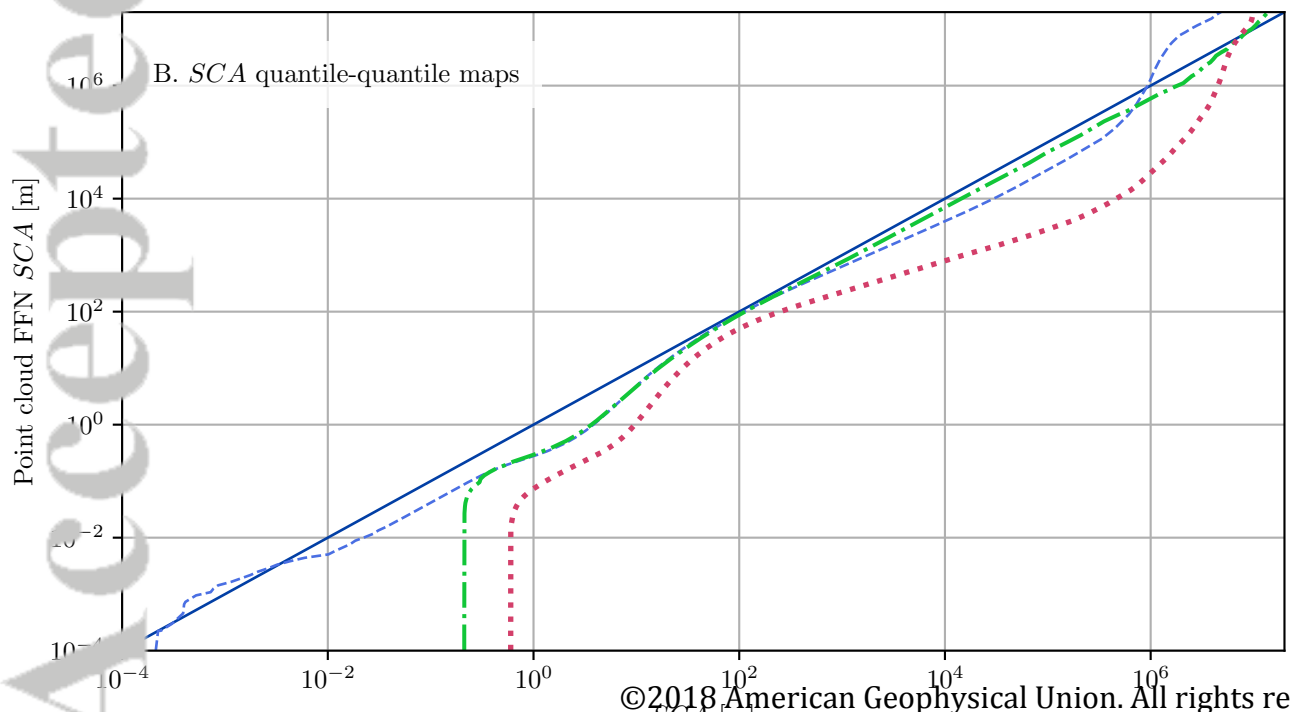
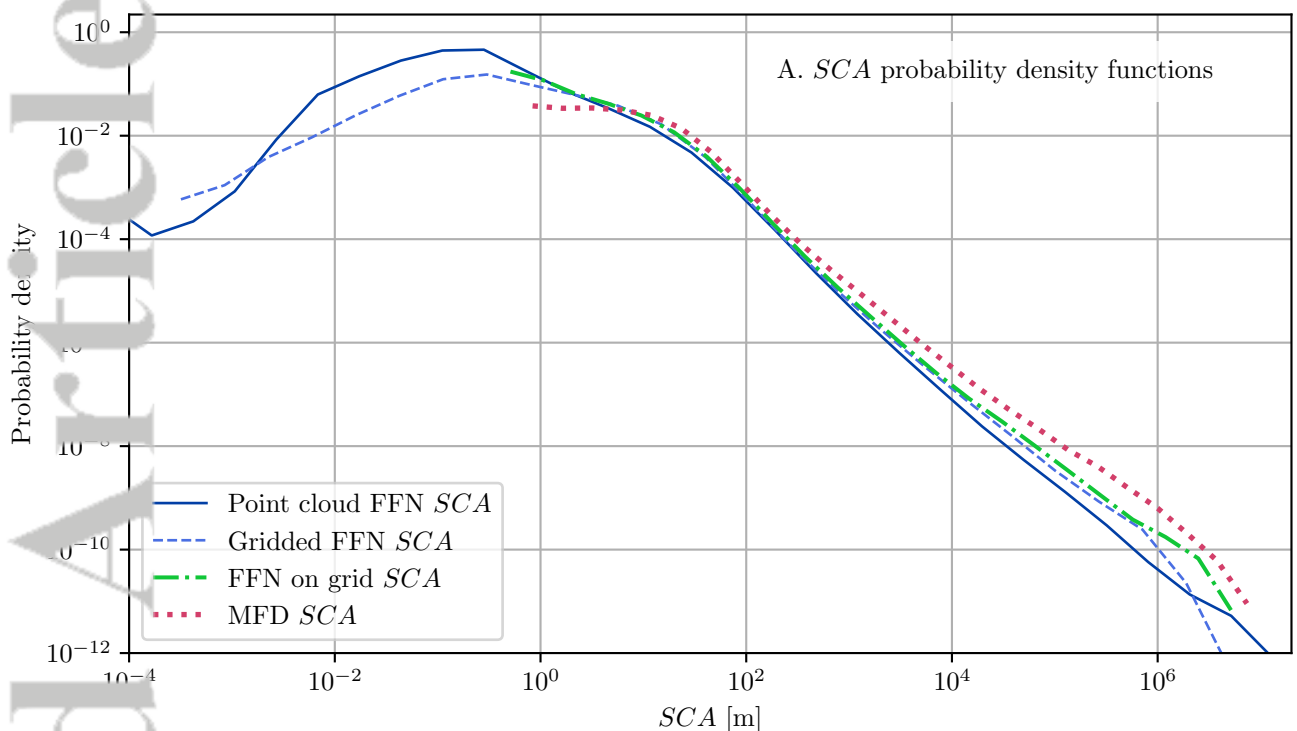


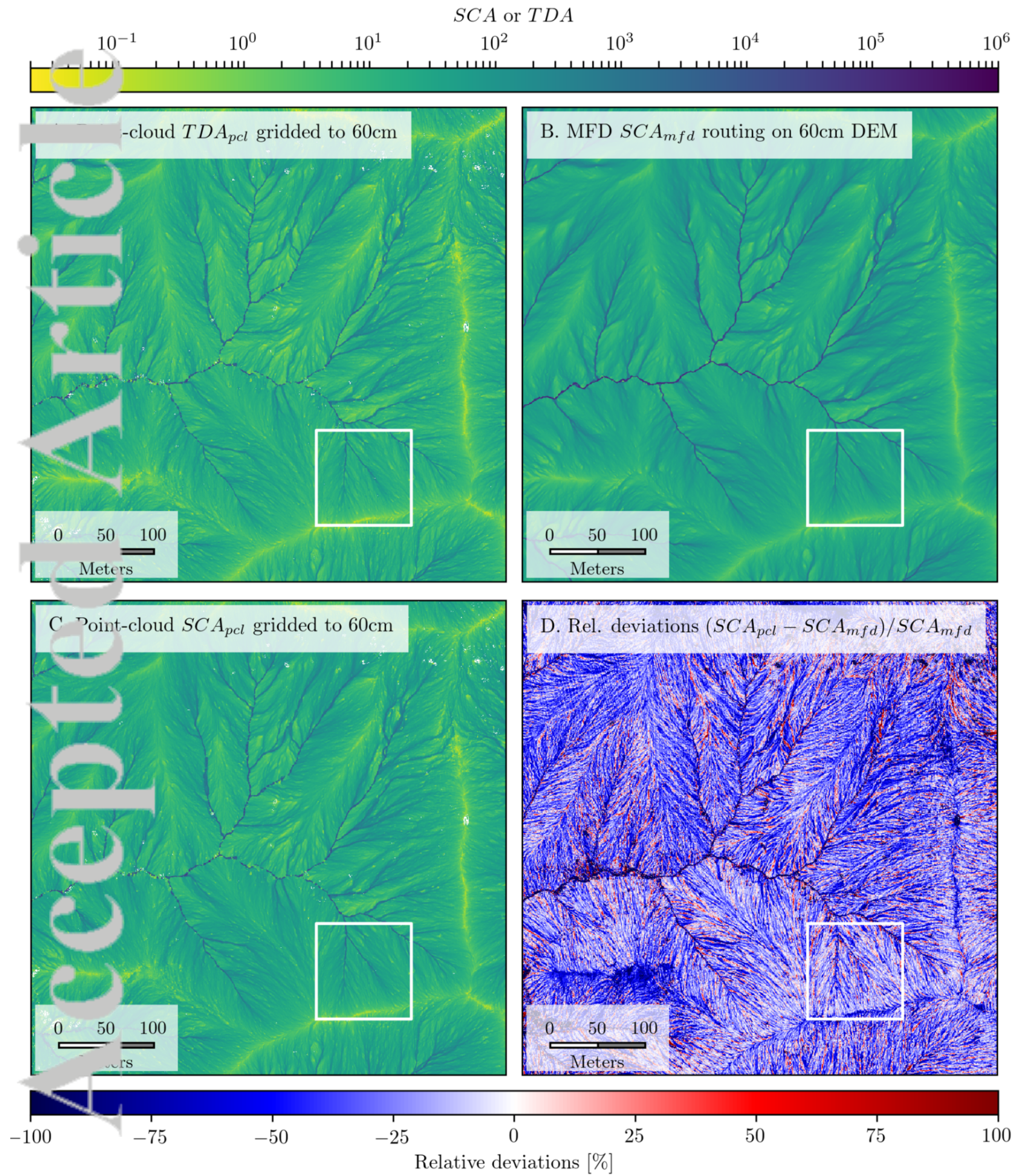
C. gridded DEM from point cloud



D. gridded version of B

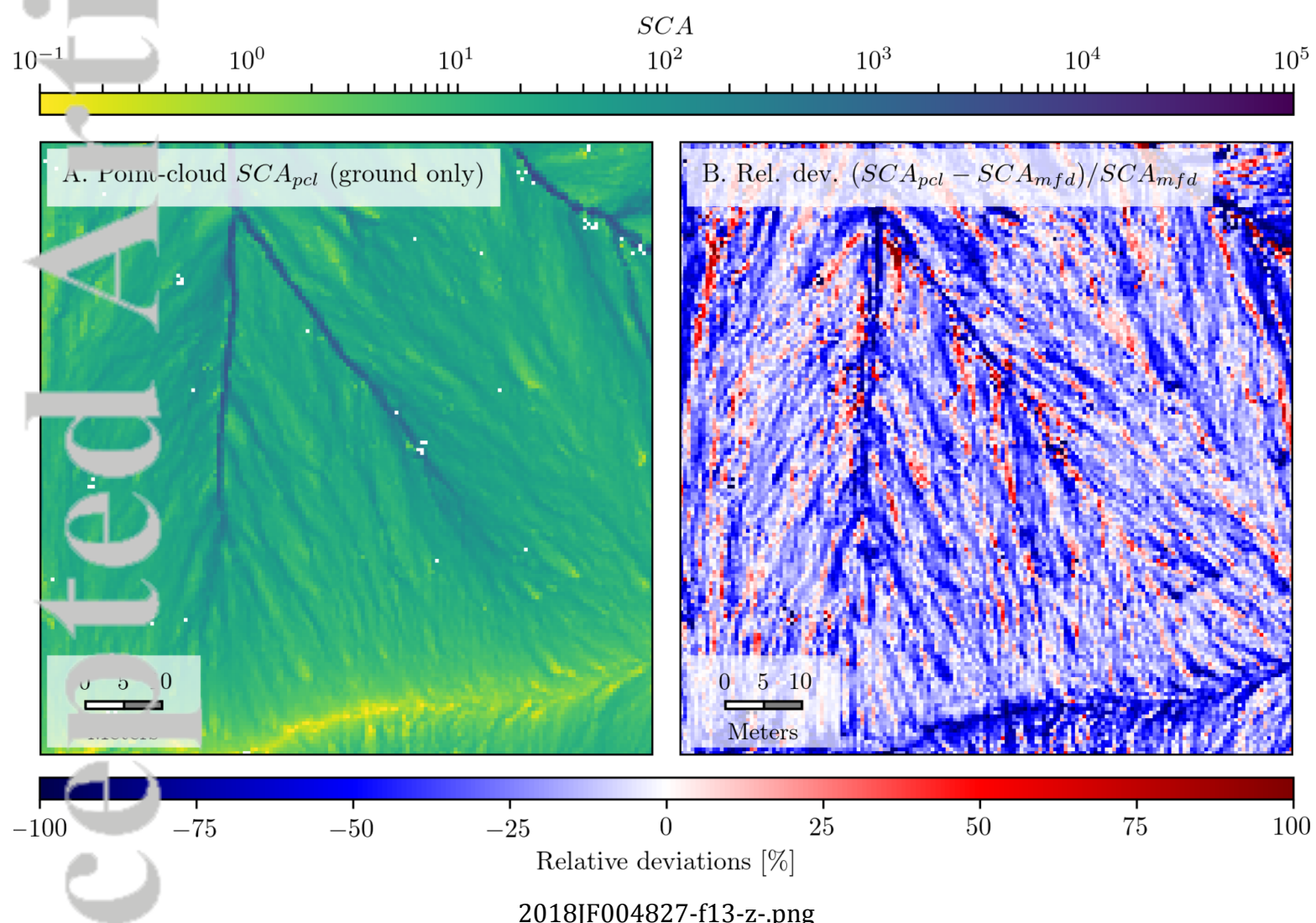


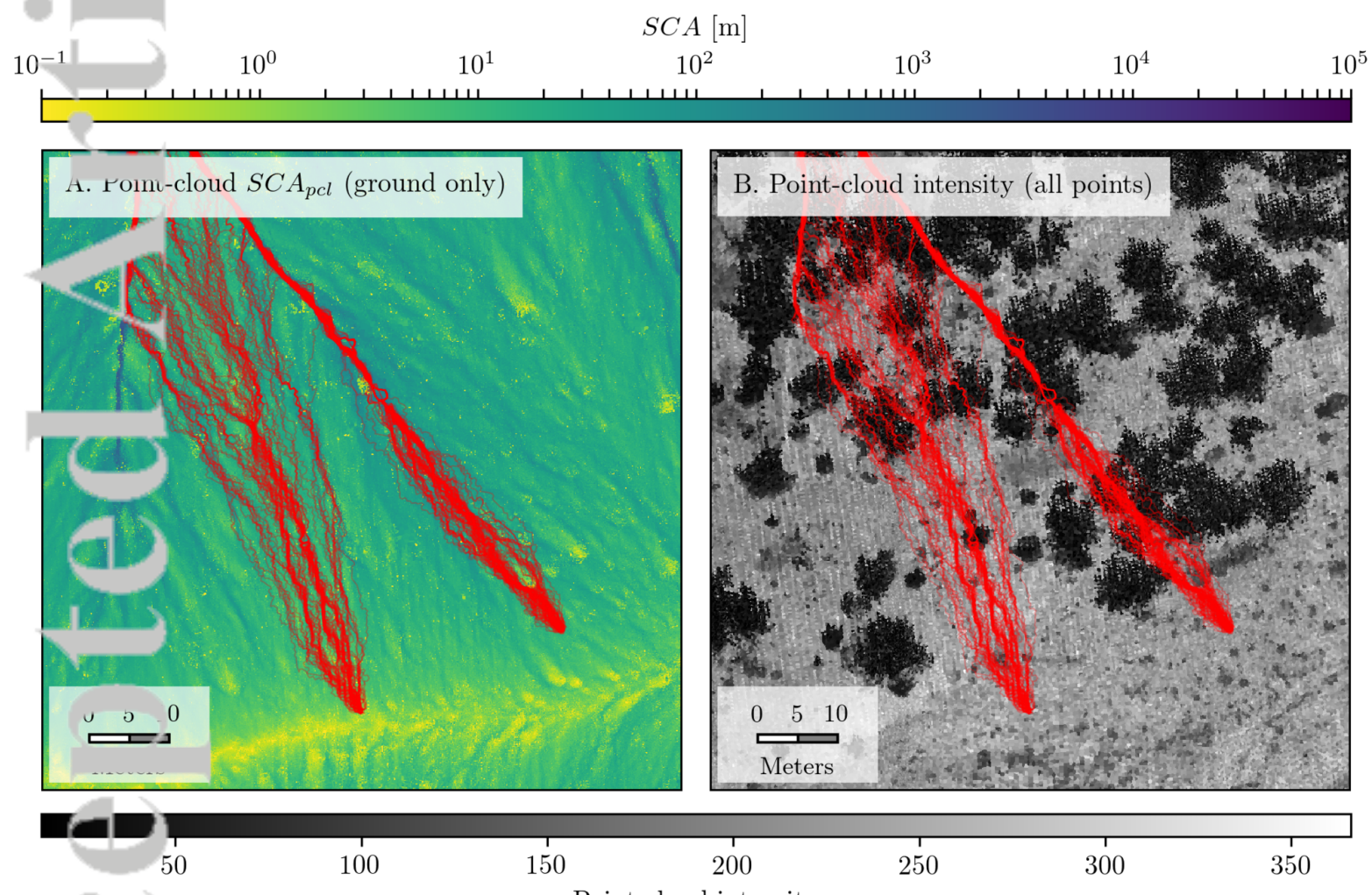




2018JF004827-f12-z-.png

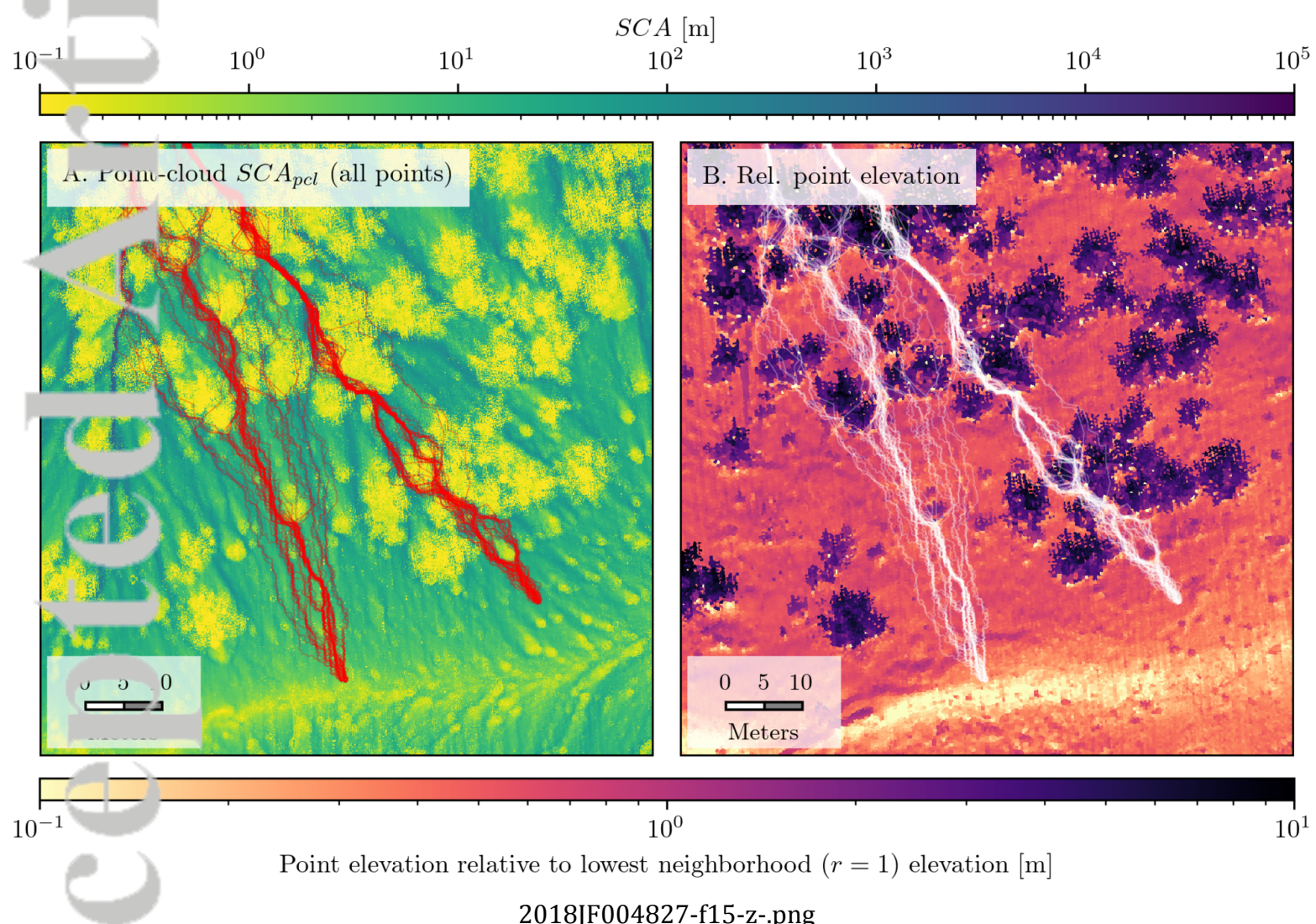
Accepted Article





2018JF004827-f14-z-.png

Accepted Article



2018JF004827-f15-z-.png

MFD elevation
Point cloud FFN elevation

Point cloud FFN *SCA*
IQR of surrounding elevations

